

LOWER HYBRID WAVES GENERATED IN THE
WAKE OF THE GALILEO SPACECRAFT

by

Andrew Edward Keller

An Abstract

Of a thesis submitted in partial fulfillment
of the requirements for the Doctor
of Philosophy degree in Physics
in the Graduate College of
The University of Iowa

December 1995

Thesis supervisor: Professor Donald A. Gurnett

ABSTRACT

During the first flyby of Earth by the Galileo spacecraft, which occurred on December 8, 1990, spin-modulated bursts of broadband electrostatic noise were observed with an intensification near the local lower hybrid frequency. These bursts occurred while the spacecraft was passing through the plasmasphere, where both the plasma density and the magnetic field strength are relatively high. By analyzing the spin modulation, which consisted of one burst per spacecraft rotation, we have been able to show that the waves are generated in the spacecraft wake. To explain the observations, we suggest that plasma density gradients in the wake produce the waves via the electrostatic lower-hybrid-drift instability (LHDI). The LHDI is a consequence of the coupling between the $\vec{E} \times \vec{B}$ -drift wave, which is driven by an electric field associated with plasma density gradients, and the lower hybrid wave. The coupling occurs by means of the diamagnetic drift induced by the plasma density gradient across the magnetic field. Numerical solutions of the dispersion relation show that strong wave growth occurs over a broad frequency range, with a peak growth rate near the lower hybrid resonance frequency. The numerical analysis demonstrates that the LHDI occurs over a wide range of plasma parameters, including those that are believed to exist in the wake. These results also suggest that lower hybrid waves previously believed by other researchers to be of natural origin may in fact have been generated in spacecraft wakes via the LHDI mechanism.

Abstract approved: Dale A. Humett
Thesis supervisor

Professor, Physics and Astronomy
Title and department

Dec 4, 1995
Date

LOWER HYBRID WAVES GENERATED IN THE
WAKE OF THE GALILEO SPACECRAFT

by

Andrew Edward Keller

A thesis submitted in partial fulfillment
of the requirements for the Doctor
of Philosophy degree in Physics
in the Graduate College of
The University of Iowa

December 1995

Thesis supervisor: Professor Donald A. Gurnett

Copyright by
ANDREW EDWARD KELLER
1995
All Rights Reserved

Graduate College
The University of Iowa
Iowa City, Iowa

CERTIFICATE OF APPROVAL

PH.D. THESIS

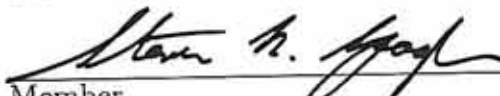
This is to certify that the Ph.D. thesis of

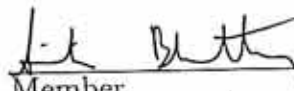
Andrew Edward Keller

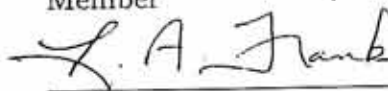
has been approved by the Examining Committee
for the thesis requirement for the Doctor of
Philosophy degree in Physics at the December 1995
graduation.


Thesis committee:


Thesis supervisor


Member


Member


Member


Member


Member

At what point in time can a man be fixed and frozen
if he is to live and grow?

- from *A Dream Within a Dream*, by John T. Dugan

ACKNOWLEDGMENTS

I wish to thank Professor Don Gurnett, Dr. Bill Kurth, Professor Amitava Bhattacharjee, and Dr. Ying Yuan for all their generous support and assistance in finding out just what went on to produce these waves and direct them to the antenna. I also wish to thank Larry Granroth, Joe Groene, Scott Allendorf, Julie Dowell, Terry Averkamp, Dr. Don Kirchner, and Dr. George Hospodarsky for all their aid in working through the maze of programming and data manipulation that was necessary in order to determine what the numbers really meant and to correlate and present them in a form that accurately reflected the truth. I must also thank my birth family, my martial arts family, and all my much-loved and under-appreciated friends; for, without you all, I could not have risen to where I stand today. Finally, if I have missed anyone else through my own forgetfulness, know that your support is deeply appreciated. This research is supported by Contract 958779 with the Jet Propulsion Laboratory and the Air Force Office of Scientific Research.

ABSTRACT

During the first flyby of Earth by the Galileo spacecraft, which occurred on December 8, 1990, spin-modulated bursts of broadband electrostatic noise were observed with an intensification near the local lower hybrid frequency. These bursts occurred while the spacecraft was passing through the plasmasphere, where both the plasma density and the magnetic field strength are relatively high. By analyzing the spin modulation, which consisted of one burst per spacecraft rotation, we have been able to show that the waves are generated in the spacecraft wake. To explain the observations, we suggest that plasma density gradients in the wake produce the waves via the electrostatic lower-hybrid-drift instability (LHDI). The LHDI is a consequence of the coupling between the $\vec{E} \times \vec{B}$ -drift wave, which is driven by an electric field associated with plasma density gradients, and the lower hybrid wave. The coupling occurs by means of the diamagnetic drift induced by the plasma density gradient across the magnetic field. Numerical solutions of the dispersion relation show that strong wave growth occurs over a broad frequency range, with a peak growth rate near the lower hybrid resonance frequency. The numerical analysis demonstrates that the LHDI occurs over a wide range of plasma parameters, including those that are believed to exist in the wake. These results also suggest that lower hybrid waves previously believed by other researchers to be of natural origin may in fact have been generated in spacecraft wakes via the LHDI mechanism.

TABLE OF CONTENTS

	Page
LIST OF FIGURES	vi
CHAPTER	
I. INTRODUCTION	1
II. SPACECRAFT TRAJECTORY AND INSTRUMENTATION	3
III. OBSERVATIONS	6
IV. ORIGIN OF THE ROTATIONAL MODULATION	13
The Wake Source Hypothesis	14
The Angular Spread of the Modulation Pattern	17
Beamwidth	18
Wavelength and Antenna Length	18
Wake Diameter	19
Offset from the Wake Axis	23
V. GENERATION MECHANISM	25
The Lower-Hybrid-Drift Instability	25
The Doppler Shift	30
VI. CONCLUSIONS	33
REFERENCES	38
APPENDIX A. ESTIMATION OF THE $\cos \phi$ FACTOR	42
APPENDIX B. FIGURES	48

LIST OF FIGURES

Figure	Page
1. The Galileo Earth-1 flyby trajectory, in Geocentric Solar Magnetospheric (GSM) coordinates, projected onto the $x - y$ plane in the top panel and the $x - z$ plane in the bottom panel.	49
2. A drawing of the Galileo spacecraft, showing the locations of the electric dipole at the end of the 10.6-meter boom, the magnetic search coil antenna, the bus shield, and the Radioisotope Thermoelectric Generators (RTGs).	51
3. A diagram showing the scheme for sampling the outputs from the medium-frequency spectrum analyzer channels.	53
4. A frequency-time spectrogram of wave electric spectral density from the step-frequency receiver during the Earth-1 flyby.	55
5. A wideband frequency-time spectrogram taken well before closest approach.	57
6. A wideband frequency-time spectrogram density taken shortly after closest approach, displayed in a format exactly similar to Fig. 5.	59
7. A wideband frequency-time spectrogram taken well after closest approach in a format exactly similar to Fig. 5.	61
8. A wideband frequency-time spectrogram similar to Figures 5, 6, and 7, but with the time scale compressed to show all of the wideband measurements taken in the region around closest approach, from 2014 UT to 2104 UT.	63

9.	A sketch of a magnetic field line linking Galileo's electric antenna to the spacecraft's wake.	65
10.	Two views, looking parallel and perpendicular to the spin axis, showing the geometry at the time that the magnetic field line through the antenna intersects the wake axis.	67
11.	The spectrogram in the top panel shows the broadband electric field strength as a function of the spacecraft rotation angle and time.	69
12.	Side views of the (a) cylindrical and (b) conical wake models.	71
13.	The spectrogram in the top panel is exactly similar to that in the top panel of Fig. 11, and the white lines give the rotation angles at which magnetic field lines through the electric antenna intersect the cylindrical wake.	73
14.	The spectrogram in the top panel is exactly similar to that in the top panel of Fig. 11, and the white lines give the rotation angles at which magnetic field lines through the electric antenna intersect the conical wake.	75
15.	A side view of the cylindrical wake model, depicting the significant wake intersection geometries.	77
16.	A plot showing the frequency (open squares) and growth rate (solid dots) for the electrostatic lower-hybrid-drift instability (LHDI) as a function of the ratio of parallel to perpendicular wavenumbers.	79
17.	A plot showing the computed frequency (open squares) and growth rate (solid dots) as a function of $k_y \rho_e$ for the electrostatic LHDI.	81
18.	A plot showing the frequency (open squares) and growth rate (solid dots) for the electrostatic LHDI as a function of the diamagnetic drift speed.	83

19. A plot showing the frequency (open squares) and growth rate (solid dots) for the electrostatic LHDI as a function of the $\vec{E} \times \vec{B}$ -drift speed. 85
20. A plot showing the maximum value of the Doppler shift $\cos \phi$ factor as a function of time (in UT) assuming the lower hybrid wave \vec{k} is unchanged. 87

CHAPTER I

INTRODUCTION

The Galileo spacecraft, which is on its way to Jupiter, made two flybys of Earth, the first on December 8, 1990, and the second on December 8, 1992. During the first Earth flyby, the plasma wave instrument detected an unusual type of broadband plasma wave emission with characteristics that have never been previously reported. The emission occurred relatively close to the Earth (< 3 Earth radii) and had a maximum intensity near the lower hybrid resonance frequency. The unique, new characteristic of this emission is that the electric field intensity is modulated at the spacecraft rotation rate, with one peak per rotation. This modulation pattern is not consistent with any known naturally occurring magnetospheric wave field. The Galileo plasma wave instrument is unusual in that the dipole electric antenna is mounted on the end of a long boom at a distance of 10.6 meters from the center of the spacecraft body. Subsequent analysis has shown that the maximum electric field intensities occur when the spacecraft is oriented such that the Earth's magnetic field connects the electric antenna to the downstream wake. Thus, it appears that the waves are generated in the spacecraft wake.

The purpose of this thesis is to describe the wake-induced waves detected by Galileo and to propose a mechanism for their generation. We begin with a brief discussion of the spacecraft trajectory during the first Earth flyby and a descrip-

tion of the plasma wave instrumentation in Chapter II. Chapter III follows with a description of the measurements. In Chapter IV, the methods for determining the location of the source are discussed, including two simple wake models that help refine the geometry of the emission region. Chapter V proposes a mechanism for generating the waves, and Chapter VI concludes by commenting on some of the questions raised, including the possibility that waves previously detected by other spacecraft near the lower hybrid resonance frequency may in fact be generated by similar wake-induced instabilities.

CHAPTER II

SPACECRAFT TRAJECTORY AND INSTRUMENTATION

The primary period of interest in this thesis is the first Galileo flyby of the Earth, which occurred on December 8, 1990. Although similar waves were detected during the second flyby, the emissions were weaker and more difficult to identify, so we have concentrated our analysis entirely on the first flyby. The spacecraft trajectory during the first flyby is shown in Figure 1 using Geocentric Solar Magnetospheric (GSM) coordinates. The x -axis in this coordinate system is directed toward the Sun, and the magnetic moment of the Earth is in the x - z plane. The y -axis completes the right-handed coordinate system. The upper panel shows a projection of the trajectory onto the x - y_{GSM} plane, and the lower panel shows a projection of the trajectory onto the x - z_{GSM} plane. The vertical and horizontal scales are marked at intervals of 2 Earth radii (R_E). As can be seen, the spacecraft approached the Earth from near local midnight, passed by the Earth at a closest approach altitude of 964 km at 2035 UT, and then departed on the dayside of the Earth at a local time of about 1000 Hr. This trajectory brought the spacecraft well within the plasmasphere and the ionosphere, where the plasma density is quite high ($> 100 \text{ cm}^{-3}$) and the magnetic field is relatively strong (> 0.1 Gauss). It is this region, inside of about $3 R_E$ geocentric radial distance, that is of primary interest.

The waves that are the subject of this analysis were detected by the Galileo

plasma wave instrument, sometimes abbreviated PWS, which stands for Plasma Wave Subsystem. The plasma wave sensors consist of a 6.6 m tip-to-tip electric dipole antenna, mounted on a boom 10.6 m from the center of the spacecraft body, and a search coil magnetic antenna, mounted on the high gain antenna feed. The locations of these antennas are shown in Figure 2. Signals from the electric and magnetic antennas are processed by two types of receivers: (1) a step-frequency spectrum analyzer, and (2) a wideband waveform receiver. The step-frequency spectrum analyzer provides low-resolution spectrum measurements from 5.6 Hz to 5.65 MHz and has three frequency ranges. The low-frequency range covers frequencies from 5.62 Hz to 31.1 Hz, the medium-frequency range covers frequencies from 42.1 Hz to 160.8 kHz, and the high-frequency range covers frequencies from 100.8 kHz to 5.65 MHz. The frequency-step pattern of the medium-frequency spectrum analyzer, which is of the greatest interest in this study, is shown in Figure 3. The low- and high-frequency analyzers have similar frequency step patterns. Note that the frequency sweep is logarithmic (i.e., the logarithm of the frequency increases linearly with time). The low- and medium-frequency analyzers can be connected to either the electric antenna or the magnetic antenna. In the normal mode of operation, these two analyzers cycle back and forth between the electric and magnetic antennas with a cycle time of 37.33 seconds. Since the upper frequency range of the magnetic search coil antenna does not extend into the frequency range of the high-frequency analyzer, the high-frequency analyzer remains continuously connected to the electric antenna.

The wideband receiver provides high-resolution waveform measurements and

has three frequency bands: 5 Hz to 1 kHz, 50 Hz to 10 kHz, and 50 Hz to 80 kHz. The wideband receiver can be connected to either the electric antenna or the magnetic antenna. The frequency band and antenna selection are controlled by command. Waveforms in the selected frequency band are digitized with a 4-bit analog-to-digital converter. Because of the limited dynamic range of the analog-to-digital converter, an automatic gain control is used to insure that the signal amplitude remains within the available dynamic range. The waveforms are sampled in blocks, the duration of which is determined by the receiver bandwidth and rate of data transmission. A typical block, for example in the 50 Hz to 10 kHz bandwidth mode at a bit rate of 100.8 kb/s, consists of 1,574 samples taken at a sample rate of 25,200 samples per second. A typical duration between data blocks is $66\frac{2}{3}$ milliseconds. On the ground, each block of waveform data is Fourier transformed to provide a spectrum. The spectrums from successive data blocks are then assembled into a frequency-time spectrogram, which can be used to study the temporal evolution of plasma wave phenomena on a very fine time scale. For further details on the capabilities and operation of the Galileo plasma wave instrument see *Gurnett et al.* [1992].

CHAPTER III

OBSERVATIONS

A frequency-time spectrogram of the electric field data obtained from the step-frequency spectrum analyzer during the first Earth flyby is shown in Figure 4. Frequencies are displayed logarithmically on the vertical axis starting at 42.1 Hz and ending at 5.65 MHz, and the time of day in Universal Time (UT) is displayed on the horizontal axis starting at 1930 UT and ending at 2130 UT. The geocentric radial distance to the spacecraft, in Earth radii (R_E), is given at the bottom of the plot. The time and radial distance of closest approach (C/A) are also noted. The electric field spectral density is indicated by the color scale at the top of the figure, and runs from 10^{-17} (blue) to $10^{-10} \text{ V}^2 \text{ m}^{-2} \text{ Hz}^{-1}$ (red). The spectrogram in Figure 4 shows many of the same plasma wave phenomena commonly observed by other spacecraft in the inner regions of the Earth's magnetosphere. These include upper hybrid waves (of the type reported by *Walsh et al.* [1964], *Bauer and Stone* [1968], *Gregory* [1969], *Hartz* [1969], and later studied in more detail by *Mosier et al.* [1973], and others), plasmaspheric hiss (first observed by *Russell et al.* [1969] and later studied by *Thorne et al.* [1973], *Parady and Cahill* [1973] and others), and chorus (first described by *Storey* [1953]).

The upper hybrid emissions, which occur above about 100 kHz in the region near closest approach, provide a convenient method of measuring the plasma den-

sity. The upper hybrid resonance frequency is given by $f_{UHR} = \sqrt{f_{pe}^2 + f_{ce}^2}$, where f_{pe} is the electron plasma frequency and f_{ce} is the electron cyclotron frequency. Throughout most of the region of interest, $f_{pe} \gg f_{ce}$, so $f_{UHR} \simeq f_{pe}$. Since $f_{pe} \simeq 9\sqrt{n_e}$ kHz, where n_e is the electron density in cm^{-3} , the upper hybrid resonance frequency provides a direct indication of the electron density. As one can see from Figure 4, the electron plasma frequency, hence electron density, increases abruptly from about 30 kHz ($n_e \simeq 11 \text{ cm}^{-3}$) to 150 kHz (280 cm^{-3}) at 1956 UT, rises gradually to a peak of about 2 MHz ($4.9 \times 10^4 \text{ cm}^{-3}$) near closest approach at 2034 UT, and then declines slowly to about 120 kHz (180 cm^{-3}) at 2114 UT, where it abruptly decreases back to about 30 kHz (11 cm^{-3}). The abrupt changes in the plasma density at 1956 and 2114 UT are characteristic of the entry into and the exit from the plasmasphere. The plasmasphere is a region of relatively cold corotating plasma near the Earth that has a plasma density significantly higher than other regions of the magnetosphere [Carpenter, 1963; 1966].

The plasma wave emissions that are the subject of this study appear in Figure 4 as a series of stripe-like features in the region near closest approach, from about 2045 to 2100 UT. The stripe-like features sweep upward across the spectrogram, always increasing in frequency with increasing time, and are only observed in the electric field data. The maximum electric field strengths are about $100 \mu\text{V/m}$. The stripes have several unusual characteristics. First, even though the frequency scale is logarithmic, the stripes have a linear relationship between the logarithm of the frequency and time. Second, the slope of the stripes on the log-frequency-versus-time plot is constant, independent of the spacecraft position. Since it

is highly unlikely that any naturally occurring magnetospheric phenomena could maintain the same linear log-frequency-versus-time relationship over such a large range of plasma parameters, it is highly unlikely that the stripes are indicative of the true frequency-time variation of the phenomena being detected. Instead, the linear log-frequency-versus-time characteristic suggests that the response is somehow controlled by the step-frequency receiver, which has a linear log-frequency-versus-time sweep.

The linear response of the step-frequency receiver can be explained if we assumed the signals causing the stripes are of short duration (\sim a few seconds), have a broad bandwidth, and occur only once per spacecraft rotation. To understand how a brief, broadband, once-per-rotation signal can appear as a series of linear stripe-like features in a frequency-time spectrogram, consider more closely the operation of the medium-frequency spectrum analyzer. As shown in Figure 3, the medium-frequency spectrum analyzer consists of four bands, each with 28 frequency steps. At any given time in the measurement cycle, one frequency from each band is being sampled. Each sample takes $\frac{2}{3}$ second, so the total time to go through 28 steps is 18.67 seconds. The spacecraft rotation period during the first Earth flyby was 19.07 seconds. Thus, the medium-frequency spectrum analyzer makes approximately 29 measurements during each rotation of the spacecraft. Therefore, a "beat" exists between the spacecraft rotation and the cycling of the step-frequency analyzer. A brief, broadband, once-per-rotation signal detected in analyzer steps 3-5 during one rotation would be detected in steps 4-6 during the next rotation, in steps 5-7 during the following rotation, etc. It is easy to show that the beat period, T , required

for the stripe to pass through one of the 28-channel bands of the step-frequency analyzer is given by

$$\frac{1}{T} = \left(\frac{1}{18.67 \text{ s}} - \frac{1}{19.07 \text{ s}} \right). \quad (1)$$

This formula gives a beat period of $T = 890.1$ seconds, or about 14.8 minutes. Since 28 channels correspond to a factor of eight in frequency (the full frequency range of the medium-frequency analyzer has $4 \times 28 = 112$ channels), the response on a spectrogram such as Figure 4 should be linear with a slope of three octaves (a factor of eight) in frequency per 14.8 minutes. As can be seen in Figure 4, this slope is in very good agreement with the observed slope. If one broadband burst is detected per rotation then four stripes should be observed at any one time, one for each of the 28-channel bands. As can be seen Figure 4, four stripes are usually present at any one time.

To test the beat hypothesis, the wideband waveform receiver measurements obtained during the time interval around closest approach were examined to see if a broadband burst of noise was observed once per rotation. Representative frequency-time spectrograms of the signals from the wideband receiver in the region near closest approach are shown in Figures 5, 6, and 7. Figure 5 shows the relative electric field spectral density for an interval of just over one minute on the inbound leg starting at 2016:16 UT, when Galileo was at a geocentric radial distance of about $2.3 R_E$. The frequency scale on the vertical axis of this spectrogram extends from 0 to 10 kHz, and the time scale on the horizontal axis, called Relative Time (RT), extends from 0 to 60 seconds. Relative spectral density is plotted on the color

scale shown at the top of the figure, in decibels (dB) from 0 (blue) to 40 dB (red). As can be seen, a band of enhanced emissions can be seen extending across the spectrogram at about 2 kHz. This band has clearly defined intensifications at 14 s, 33 s, and 52 s RT. The interval between these intensifications (~ 19 s) is almost exactly the spacecraft rotation period. The band of enhanced emission at about 2 kHz is frequently observed in the ionosphere and plasmasphere and is known to be associated with the lower hybrid resonance frequency [see *Brice and Smith*, 1965; *McEwen and Barrington*, 1967; *Storey and Cerisier*, 1968; *Gurnett et al.*, 1969]. For a sufficiently dense plasma with a single ion species, the lower hybrid resonance frequency is given by $f_{LHR} = \sqrt{f_{ce}f_{ci}}$, where f_{ce} is the electron cyclotron frequency and f_{ci} is the ion cyclotron frequency. At the relatively high altitude (8,300 km) where these observations were made, the dominant ion is expected to be H^+ . The lower hybrid resonance frequency computed assuming a pure H^+ plasma is shown by the white line in Figure 5. As can be seen, the band of enhanced emission is centered almost exactly on the lower hybrid resonance frequency. Usually the lower hybrid resonance frequency corresponds to the lower cutoff of the band of enhanced emission. One can see from Figure 5 that the lower cutoff is a few hundred Hertz below the computed lower hybrid resonance frequency. This slight discrepancy is not surprising since the lower hybrid resonance frequency was computed assuming a pure H^+ plasma. In the plasmasphere heavier ions, especially O^+ , are expected to be present. The presence of these heavier ions causes the lower hybrid resonance frequency to be somewhat lower than for a pure H^+ plasma.

Figure 6 shows another wideband frequency-time spectrogram starting at

2044:40 UT, shortly after closest approach, when Galileo was about at a geocentric radial distance of $1.6 R_E$. This spectrogram uses the same color scale and frequency-time scale as Figure 5. In this case, a very strong once-per-rotation modulation can be seen, with bursts at 18 s, 37 s, and 56 s RT, again centered on the lower hybrid resonance frequency. The lower hybrid resonance frequency (computed assuming a pure H^+ plasma) is shown by the white line. Figure 7 shows another example of the once-per-rotation bursts at about 2059:14 UT, when Galileo was at a radial distance of about $2.9 R_E$ on the outbound leg. The electric field spectral densities are again displayed using the same color scale and format as Figure 5, except that the frequencies now extend from 0 to 80 kHz. As can be seen, a series of broadband bursts appears at ~ 19 s, 38 s, and 57 s RT. The time interval between these bursts is almost exactly the spacecraft spin period. The bursts have a very broad bandwidth, with frequencies extending from near the lower hybrid frequency, which is at about 1 kHz, to as high as 60 kHz. As in the previous examples, the highest intensities occur near the lower hybrid resonance frequency.

An examination of all the wideband spectrograms recorded during the first Earth flyby shows two periods where a strong once-per-spin modulation appeared, the first from 2014 to 2031 UT, and the second from 2041 to 2104 UT. These two intervals are separated by a data gap from about 2031 to 2041 UT. Since the stripe-like features were observed in the step-frequency receiver through the gap in the wideband data, it is likely that the once-per-spin bursts occurred continuously over the entire interval from 2014 to 2104 UT. The frequency spectrum of the signals detected by the wideband receiver through the entire pass is summarized in Figure 8.

This spectrogram is similar to Figure 5, but the time scale has been compressed so that the entire interval from 2014 to 2104 UT is displayed. As can be seen, the electric field spectrum has a well-defined enhancement at a frequency that closely tracks the lower hybrid resonance frequency, shifting steadily upward in frequency on the inbound pass, from about 2 kHz at 2015 UT to about 10 kHz at 2028 UT, and shifting steadily downward in frequency on the outbound pass, from about 6 kHz at 2042 UT to about 1.5 kHz at 2055 UT. The vertical spike-like features evident on a fine time scale (~ 19 s) are caused by the once-per-rotation modulation.

CHAPTER IV

ORIGIN OF THE ROTATIONAL MODULATION

It is well known that the response of an electric dipole antenna rotating in a constant amplitude wave field has a characteristic twice-per-rotation modulation. The maximum response occurs when the axis of the antenna is parallel to the electric field, and the minimum response occurs when the antenna axis is perpendicular to the electric field. As the spacecraft rotates, the antenna axis passes through perpendicular twice each rotation, which gives rise to the characteristic twice-per-rotation modulation. For wavelengths long compared to the length of the antenna, it is easy to show that the intensity varies as $\cos^2 \theta$, where θ is an angle that characterizes the rotational orientation of the antenna. Since the Galileo electric antenna is mounted on the end of a long boom, the antenna essentially acts as a probe that surveys the wave intensity in a circular arc around the spacecraft. The fact that only one peak occurs per rotation can mean either that the waves are generated only during a certain phase of the spacecraft rotation, or that the waves are generated continuously, but are confined to a localized beam that is traversed once per rotation. In either case, the once-per-rotation modulation implies that waves must be generated in the near vicinity of the spacecraft. The key issues then have to do with the location of the source, the mode of propagation, and the mechanism by which the waves are generated.

In the process of carrying out this study, several models were considered to explain the once-per-rotation modulation. These include: (1) electrical discharges produced by spacecraft charging effects, (2) instabilities produced by pick-up ions from propellant leaks or other unknown gas sources, and (3) instabilities generated in the plasma wake of the spacecraft. Of these, the plasma wake model provides a source that is consistent with all of the available observations. The remainder of the chapter is devoted to a discussion of this model, which is called the wake source hypothesis.

The Wake Source Hypothesis

Since the emissions are strongest near the lower hybrid resonance frequency, there are good reasons to believe the waves are propagating in the lower hybrid mode. The lower hybrid mode is a limiting case of the whistler mode [Stix, 1962]. For frequencies near the lower hybrid resonance, the wavelengths become very small at wave normal angles near the resonance cone and the fields become electrostatic. An important property of the lower hybrid mode is that the wave energy (i.e., the group velocity) is guided very nearly along the magnetic field. For a discussion of this guiding effect, see Mosier and Gurnett [1969]. Since lower hybrid waves are guided very closely along the magnetic field, a simple test can be performed to determine if the source is located in the downstream wake region. If the waves are generated in the wake, then the maximum intensities should occur when the magnetic field through the electric antenna intersects the wake. The geometry involved is illustrated in Figure 9. Note that as the spacecraft rotates there is only one orientation that produces a magnetic connection between the center of

the electric antenna and the wake axis. Thus, there should be only one peak per rotation, which is the defining characteristic of the stripe-like emissions.

To carry out a quantitative test of the wake source hypothesis, a suitable coordinate system must be used to analyze the spin modulation. For this purpose, it is convenient to define a rotation angle, ϕ , which is the angle between the boom that carries the electric dipole antenna and the projection, \vec{B}_\perp , of the magnetic field onto a plane perpendicular to the spin axis. This angle is measured positive from the magnetic field in the direction of rotation. At some phase of the rotation, $\phi = \phi_{wake}$, the magnetic field line through the center of the antenna intersects the wake axis. The geometry at this instant in time is illustrated in Figure 10. The upper panel shows a view looking along the spin axis, and the lower panel shows a view looking perpendicular to the spin axis. In general, the wake axis is not aligned along the spacecraft spin axis, so the magnetic field/wake intersection is offset to one side as shown in the upper panel. To determine the orientation of the wake axis, it is necessary to compute the spacecraft velocity, $\vec{V}_{s/c}$, relative to the plasma. The computation of $\vec{V}_{s/c}$ must take into account the fact that the plasma within the plasmasphere corotates with the Earth. From knowledge of the wake axis orientation, the spin axis orientation (which was directed toward the Sun), and the magnetic field direction, it is a straightforward matter to compute the angle ϕ_{wake} . Since the downstream location of the intersection is also potentially important, the distance δ_{wake} at which the magnetic field line intersects the wake axis was also computed. This distance is measured along the wake axis from the center of the spacecraft body as shown in the bottom panel of Figure 10.

To compare the observations with the predictions of the wake source hypothesis, a spectrogram display was developed that shows the broadband electric field strength as a function of the spacecraft rotation angle, ϕ , and time. A spectrogram of this type is shown in the top panel of Figure 11. The vertical axis gives the rotation angle in degrees, and the horizontal axis gives the time in UT using the same scale as in Figure 8. The color at any given point in the spectrogram shows the electric field strength, which ranges from 3×10^{-7} (blue) to 10^{-4} V m⁻¹ (red). The electric field strength was calculated from the wideband receiver data. To restrict the response to the part of the spectrum where the once-per-rotation modulation is the strongest, and to suppress unwanted magnetospheric emissions, the electric field strength was computed by integrating the wideband spectrums from 1 kHz to 9 kHz. As described earlier, one wideband spectrum can be computed from each 66.7 ms data block. Since the wideband receiver has an automatic gain control (AGC), it was also necessary to take into account variations in the AGC gain. The AGC gain is sampled once every 2.67 s and has a time constant of 0.1 s. To provide AGC gain values on a time scale consistent with the 66.7 ms spectrum integration interval, the AGC gain was interpolated between the 2.67 s samples using a spline routine. Using this procedure a total of 287 electric field strength values were obtained per spacecraft rotation. These values were then used to generate one vertical line in the spectrogram, thereby giving a time resolution corresponding to one rotation, or about 19 s. As can be seen, the peak broadband electric field strength of the spin modulated noise is about 10^{-4} V/m.

In Figure 11, the rotational angle, ϕ_{wake} , at which the magnetic field line

through the center of the electric antenna intersects the wake axis, is indicated by the solid white line. The abrupt 180° discontinuity in ϕ_{wake} at 2032:20 UT, and again at 2049:50 UT, occurs as the magnetic field passes through the spin plane. Note that δ_{wake} goes to zero at these two times. Considerable scatter exists in the electric field strengths on the left-hand side of the spectrogram, with peaks sometimes occurring at random angles. Inspections of the wideband spectrograms during this interval show that the random peaks are caused by whistlers, chorus, and other naturally occurring magnetospheric emissions. On the right-hand side of the spectrogram, the scatter is much smaller with one main peak that closely tracks the wake-intersection line. Overall, the close agreement between the location of the once-per-rotation peak and the wake-intersection line gives strong support for the wake source hypothesis.

The Angular Spread of the Modulation Pattern

It is evident from the spectrogram in Figure 11 that the peak in the modulation pattern extends over a considerable range of angles, on the order of $\Delta\phi \simeq 30^\circ$ to 40° . At the center of the electric antenna, which is located on the end of the long boom, this angular spread corresponds to an arc length of about 6 meters. Several factors have been considered that could in principle contribute to this angular spread. These include (1) the beamwidth relative to the magnetic field, (2) the finite wavelength and antenna length, and (3) the finite diameter of the wake. Each of these factors is now considered in detail.

Beamwidth

For lower hybrid waves, the wave energy propagates in a cone of directions around the magnetic field that is determined by the resonance cone angle. For frequencies near the lower hybrid resonance frequency, it is easily shown [Gurnett *et al.*, 1979] that the angle, ψ , between the direction of energy propagation (group velocity) and the magnetic field is given to a good approximation by the equation

$$\tan^2 \psi = \frac{f^2 - f_{LHR}^2}{f_{ce}^2}, \quad (2)$$

where f is the wave frequency, f_{LHR} is the lower hybrid resonance frequency, and f_{ce} is the electron cyclotron frequency. This equation is valid in the high-density limit, $f_{pe}^2 \gg f_{ce}^2$, a condition that is usually satisfied in the region of interest. For $f = f_{LHR}$, the above equation shows that the wave energy is guided exactly along the magnetic field ($\psi = 0$). Since $f_{ce}^2 \gg f_{LHR}^2$, one can see that ψ is small even if f is substantially greater than f_{LHR} . For example, if $f = 2f_{LHR}$, $\psi \simeq 2.3^\circ$, and if $f = 5f_{LHR}$, $\psi \simeq 6.5^\circ$. These calculations show that the beaming angles are much smaller than the observed angular spread, so finite beamwidth effects do not play a role in determining the angular spread of the modulation pattern.

Wavelength and Antenna Length

It is well known that the transverse width of a beam of radiation cannot be smaller than the wavelength of the waves that make up the beam. The fact that the spin-modulated emissions are confined to a small arc (~ 6 m) of the antenna motion shows that the wavelengths must be quite small, not more than a few meters. On the other hand, the wavelengths cannot be too small, because the antenna would

then not respond to the electric field. For a cylindrical dipole antenna, it is easily shown that the antenna response (received intensity/incident intensity) varies as $(\sin x/x)^4$, where $x = \pi(L/2)/\lambda$, L is the tip-to-tip length of the antenna, and λ is the wavelength [Fuselier and Gurnett, 1984]. Although the exact ratio of the incident intensity to the received intensity is not known, one can see from the above equation that the antenna response decreases very rapidly when the wavelengths are less than about $L/2$. Since $L/2$ for the Galileo antenna is approximately 3.3 m, the wavelengths probably cannot be much less than 1 m, and almost certainly not less than 0.1 m. This gives us a well defined upper and lower limits to the wavelength of the burst emissions.

Wake Diameter

Since the spacecraft body has a finite size, it is clear that the wake cannot be simply represented by a line as was done in Figures 9 and 10. To take into account the finite size of the wake, one must consider the geometry of the wake. In the absence of direct measurements of the wake region, we have relied upon two mathematical models to approximate the expected boundaries of the wake region.

The first wake model, to be called the cylindrical wake, assumes that the spacecraft sweeps out a cylindrical "hole" in the plasma downstream of the spacecraft, the diameter of which is determined by the transverse dimensions of the spacecraft body. Because of thermal motions in the plasma, the wake is not expected to maintain the simple cylindrical configuration described by the cylindrical wake, but should rather close in a conical configuration downstream of the spacecraft [Katz *et al.*, 1985]. This led us to develop a second wake model by adding a closure term to

the cylindrical wake. To determine a reasonable rate of closure, we considered only the thermal motion of the particles. Electrons, due to their lower mass and consequently higher thermal speed, start to fill the wake first. However, a self-regulating, retarding ambipolar electric field (pointing toward the wake axis) develops from the charge separation, slowing the electrons' entry into the wake until the ions can catch up. Thus, it is the ions' thermal speed that provides a first-order estimate to the closure rate. The addition of the ion thermal speed to the cylindrical wake model defines the second wake model, which will be called the conical wake. *Stone et al.* [1988] has shown that real wakes actually collapse a little faster than the conical wake, but the ion thermal speed provides a realistic, yet simple estimate of the closure rate for the model. In general, the wake axis is not aligned along the spacecraft spin axis, so the cylindrical wake would appear as shown in Figure 12a, and the conical wake would appear as in Figure 12b. With either model, the finite size of the wake is primarily determined by the spacecraft body. The largest object on the spacecraft body is the bus shield (see Figure 2), which has a diameter of 4.2 m. The diameter of the wake is therefore taken to be 4.2 m. The half-angle of the conical wake cone is given by $\arctan(v_{ith}/V_{s/c})$, where v_{ith} is the thermal speed of the ions and $V_{s/c}$ is again the spacecraft speed relative to the plasma. If the ions are H^+ at a temperature of about $3000^\circ K$, which is typical for the upper levels of the Earth's ionosphere, the half-angle of the wake cone should be approximately 20° . For this half-angle the wake cone would extend about 6 m downstream of the spacecraft. For heavier ions, such as O^+ , which are more abundant at lower altitudes, the half-angle would decrease by a factor of four, to about 5° , which means that the wake

cone could then extend as much as 24 meters downstream of the spacecraft. These estimates of the downstream dimensions of the wake are generally consistent with the range of δ_{wake} values sampled during the flyby. As can be seen from Figure 11, the distance δ_{wake} to the downstream wake intersection had a maximum value of about 12 m.

To compare the spin modulation pattern with the cylindrical and conical wake models, dotted and dot-dashed lines are shown in the upper panels of Figures 13 and 14 that represent the rotation angles at which the magnetic field line through a specific part of the antenna intersects the boundaries of a model wake. The same dotted and dot-dashed coding is used in Figs. 12, 13, 14, and 15. Figure 15 is shown to help define the meaning of each line shown in Figures 13 and 14. The four antennas shown in this figure are actually projections of the antenna along magnetic field lines into the plane of the dotted and dot-dashed boundary lines of the cylindrical wake. Each antenna projection shown occurs at a specific time in the rotation of the antenna about the spacecraft, and each occurs at a time different from the other projections shown.

In Fig. 15, antenna projections (b) and (c) correspond to the intersection of a magnetic field line through the center of the antenna with the dot-dashed and dotted lines, respectively. The rotation angles at which the intersections corresponding to antenna projection (b) occur have been plotted on Figs. 13 and 14 with a heavy dot-dashed line. Similarly, the rotation angles at which the intersections corresponding to antenna projection (c) occur have been plotted on Figs. 13 and 14 with a heavy dotted line. Antenna projections (a) and (d) correspond to the intersection of a

magnetic field line through a tip of the antenna with the dot-dashed and dotted lines, respectively, and no other part of the antenna projection intersects the wake region (between the dotted and dot-dashed lines). The rotation angles at which the intersections corresponding to antenna projection (a) occur have been plotted on Figs. 13 and 14 with a light dot-dashed line. Similarly, the rotation angles at which the intersections corresponding to antenna projection (d) occur have been plotted on Figs. 13 and 14 with a light dotted line. As can be seen in Fig. 13, the rotation angle from wake entry to wake exit is typically about 60° (light dotted to light dot-dashed lines). The rotation angles between the heavy dotted and heavy dot-dashed lines, indicating magnetic connection of both antenna elements to the wake region, typically cover about 30° within this range. The larger angular width, from wake entry to exit, fairly accurately covers the angular spread of the modulation pattern. It is most likely the disagreements that appear are due to the finite wavelength and finite antenna length effects discussed earlier, both of which would act to increase the effective angular spread relative to what one would expect for a simple cylindrical wake.

Since the wake is expected to have a conical configuration, it is interesting to see if any evidence of this conical shape exists in the spin modulation pattern. As the distance δ_{wake} to the magnetic field intersection increases, the angular spread in the modulation pattern should decrease. The largest variations in the wake intersection distance, δ_{wake} , occurs on the inbound leg (see the bottom panel of Figure 14), so this region should provide the best opportunity to look for evidence of a conical configuration. Unfortunately, on the inbound leg the spin modulation

pattern is extremely noisy, which makes it extremely difficult to judge whether the angular spread varies as one would expect. On the outbound wake, the signal-to-noise ratio is much better. As can be seen from Figure 14, the angular spread in the modulation pattern decreases systematically as δ_{wake} increases, from about 50° at 2050 UT (where $\delta_{wake} = 0$ m) to about 25° at 2103 UT (where $\delta_{wake} = 5.8$ m). This variation is consistent with the expectations for the conical wake, as shown. However, it should be noted that various other parameters, such as the plasma density and magnetic field, also change significantly over this interval, so one cannot be certain that the wake geometry is the only factor that affects the angular spread.

Offset from the Wake Axis

From Figure 11 it is evident that the peak in the spin modulation pattern has a systematic offset relative to the wake intersection angle. On the inbound leg, before 2032:20 UT where the first 180° discontinuity in ϕ_{wake} occurs, the offset of the peak relative to the wake axis is positive, approximately $+10^\circ$. From 2032:20 to 2049:50 UT, between the two 180° discontinuities in ϕ_{wake} , the offset is negative, approximately -15° . On the outbound leg, after 2049:50 UT where the second 180° discontinuity occurs, the offset again becomes positive, approximately $+15^\circ$. These offsets are much larger than can be accounted for by the known integration times and the estimated errors in the attitude determination. For example, the spectrum integration time for one block of wideband data is 66.7 ms, which corresponds to only 1.3° of angular rotation. The errors in the spacecraft attitude determination are expected to be a small fraction of one degree. The fact that the sign of the offset switches in synchronism with the 180° discontinuities in ϕ_{wake} also strongly

indicates that the offset is due to a real asymmetry and not due to some gross error in the spacecraft attitude determination. Since the 180° phase shift in ϕ_{wake} occurs as the magnetic field passes through the spin plane, one can see in Figure 13 and understand from fairly simple geometric considerations that the synchronism between the change in sign of the offset and the 180° phase shift in ϕ_{wake} means that in both cases the waves are generated on the same side of the wake. To determine which side of the wake is involved, refer to Figure 10, which corresponds to the configuration before 2032:20 UT and after 2049:50 UT, when the offset was positive. As can be seen, a positive offset corresponds to a source located on the $-\vec{V}_{s/c} \times \vec{B}$ (dotted) side of the wake. From the length of the boom (10.6 m), it is easy to show that a 10 to 15° offset corresponds to a physical displacement of the source by about 1.8 to 2.7 m from the central axis of the wake (toward the $\vec{V}_{s/c} \times \vec{B}$ direction). Possible reasons for this offset are discussed in the next chapter.

CHAPTER V

GENERATION MECHANISM

The Lower – Hybrid – Drift Instability

Since we have established that the once-per-rotation bursts of electric field noise originated in the plasma wake downstream of the spacecraft, we next investigate possible instabilities that might have accounted for the generation of this noise. Since the emissions were strongest near the lower hybrid resonance frequency, and since the wake was expected to have strong plasma density gradients, one obvious possibility is the lower-hybrid-drift instability (LHDI). Three criteria must be satisfied for the LHDI to occur. These criteria are: (1) the existence of an $\vec{E} \times \vec{B}$ drift and a diamagnetic drift (*Krall and Liewer* [1971], *Gladd* [1975], *Davidson et al.* [1977]), (2) a low plasma beta (see *Yoon et al.* [1994], and references therein), and (3) a weak or negligible magnetic shear (*Krall* [1977]). All three of these conditions are satisfied in the downstream wake. The lower-hybrid-drift instability involves a drift wave, with a frequency given by $\omega = k_y v_G$, where v_G is a cross-field particle drift velocity (such as the $\vec{E} \times \vec{B}$ drift, denoted by v_E), and a lower hybrid wave, with a frequency given by $\omega = \omega_{LHR}$. The drift and lower hybrid waves are coupled by plasma density gradients, which provide the free energy source for the instability. The origin of this coupling can be seen heuristically from the equation (see *Krall and Liewer* [1971], equation (7))

$$(\omega - k_y v_E)(\omega - \omega_{LHR}) = -\frac{k_y v_{dr}}{k^2 \lambda_D^2} \frac{\omega^2}{\omega_{pi}^2}, \quad (3)$$

where ω is the wave frequency, \vec{k} is the wave number, ρ_e is the (thermal) electron gyroradius, λ_D is the Debye length, and v_{dr} is the diamagnetic drift speed. In this equation, the z -axis is along the magnetic field, the x -axis is along the density gradient, and the y -axis completes the right-handed coordinate system. It is also assumed in this equation that the wave vector is perpendicular to the magnetic field, $k_z = 0$, and that the electron gyroradius is much smaller than the wavelength, $k_y^2 \rho_e^2 \ll 1$. Instability occurs whenever the right-hand side of Equation 3 is non-zero.

In the region where the once-per-rotation bursts were observed, the ionospheric plasma has the following approximate parameters: $T_e \approx T_i \approx 3000^\circ\text{K}$, $n_e \approx n_i \approx 2.0 \times 10^{11} \text{ m}^{-3}$, and $B \simeq 10^{-5} - 10^{-4} \text{ T}$. In the rest frame of the spacecraft, the plasma streaming velocity is $v_p \simeq 10^4 \text{ m s}^{-1}$. From the above parameters, the electron and ion thermal velocities are inferred to be $v_e \approx 2 \times 10^5 \text{ m s}^{-1}$ and $v_i \approx 5 \times 10^3 \text{ m s}^{-1}$, respectively. The plasma beta is also very low, of the order 10^{-4} to 10^{-2} , which justifies the use of the electrostatic approximation.

To derive the appropriate analytical dispersion equation, we proceed by assuming the magnetic field is constant, neglecting spatial variations of the geomagnetic field over the scale of the Galileo spacecraft. One can also assume that the ambient plasma outside the wake is spatially uniform. However, a strong density gradient is expected to occur near the wake boundary. The scale length of this density gradient is defined to be $L_n \equiv -d(\ln n_e)/dx$. In the absence of detailed information on the density profile across the wake, the characteristic spatial scale for this density

variation is taken to be of the order of the dimension of the satellite, $L_n \sim 1$ m. Assuming that the density gradient is along the x -direction, the diamagnetic drift velocity associated with this density gradient is along the y -direction and can be estimated by $v_{dr} \approx \kappa T / (eBL_n)$, which is roughly $10^3 - 10^4$ m s $^{-1}$.

Once the wake is created by the motion of the spacecraft through the plasma, the electrons and ions immediately start to diffuse into the wake. Since the electrons diffuse into the region faster than the ions, a self-regulating ambipolar electric field is set up that equalizes the diffusion rates for the electrons and ions. This ambipolar electric field produces an $\vec{E} \times \vec{B}$ drift along the wake boundary. Assuming that the potential energy associated with this electric field is approximately 10% of the electron thermal energy, the $\vec{E} \times \vec{B}$ -drift speed is estimated to be on the order of 10^3 m s $^{-1}$.

Since we are considering waves with frequencies near the lower hybrid resonance frequency, it follows that $\omega_{ci} \ll \omega \ll \omega_{ce}$. Therefore, we can treat the electrons as magnetized and the ions as unmagnetized. Neglecting temperature and magnetic field gradients, the following dispersion equation can be used to describe the electrostatic LHDI (*Krall and Liewer* [1971]):

$$k^2 \lambda_D^2 = -\frac{T_e}{T_i} \left[1 + \frac{\omega}{kv_i} Z \left(\frac{\omega}{kv_i} \right) \right] - 1 + \frac{m_e}{T_e \pi^{1/2} v_e} \int_{-\infty}^{\infty} dv_z \int_0^{\infty} dv_{\perp} v_{\perp} \times J_0^2 \left(\frac{k_{\perp} v_{\perp}}{\omega_{ce}} \right) \exp \left(-\frac{v_{\perp}^2 + v_z^2}{v_e^2} \right) \left[\frac{\omega - \frac{k_y T_e}{m_e \omega_{ce}} \varepsilon'}{\omega - k_y v_E - k_z v_z} \right], \quad (4)$$

where $\varepsilon' = -d(\ln n_e)/dx - E/T_e$, $v_E = -E/B$, and $Z(\xi)$ is the plasma dispersion function. Integrating over velocity space and assuming $T_e = T_i$, we obtain

$$k^2 \lambda_D^2 + 2 + \frac{\omega}{k v_i} Z\left(\frac{\omega}{k v_i}\right) + \left[1 - \frac{k_y(v_{dr} + v_E)}{\omega}\right] \frac{\omega}{k_z v_e} Z(\zeta_e) I_0(b) \exp(-b) = 0, \quad (5)$$

where $\zeta_e \equiv (\omega - k_y v_E)/(k_z v_e)$ and $b = (1/2)k_y^2 \rho_e^2$.

To evaluate the frequency and growth rate of the unstable waves, we next solve Equation 5 numerically using parameters relevant to the plasma wake. The real part of the frequency (denoted by ω and plotted using empty squares) and the growth rate (denoted by γ and plotted using solid dots) are shown in Figure 16 as a function of k_z/k_y . As can be seen, the unstable modes have frequencies close to the lower hybrid resonance, and the maximum growth rate occurs for parallel wavenumbers (k_z) close to zero. Because the plasma is relatively cold, the wave energy propagates along the magnetic field, just as in cold plasma theory. It is easy to verify that the parallel component of the group velocity, $v_{g\parallel} = \partial\omega / \partial k_{\parallel}$, is of the order of 10^4 m s⁻¹. As the waves grow, they eventually escape into the surrounding plasma, where they propagate along the magnetic field with little or no damping. The dependence of the frequency and growth rate on the perpendicular wavenumber k_y is shown in Figure 17 for $k_z \approx 0$, $v_{dr} = 3.3 \times 10^3$ m s⁻¹, $v_E = 7.0 \times 10^3$ m s⁻¹, and $\rho_e = 0.11$ m. The maximum growth rate occurs for $k_y \rho_e \sim 1$, which is a well-known characteristic of the LHDI. The perpendicular wavelength and the real frequency at the maximum growth rate are about 0.7 m and 5.6 kHz, respectively. The range of unstable frequencies is broad and extends to several tens of kHz. Figures 18 and 19 show the frequency and growth rate versus the diamagnetic drift and $\vec{E} \times \vec{B}$ -drift speeds, respectively. In the absence of measurements of the density and electric field

profiles in the wake, Figures 18 and 19 demonstrate that the LHDI has high growth rates over a wide range of physical parameters, including those that are expected to occur in the wake.

In the absence of density gradients, there is another branch of the dispersion equation that also deserves attention. This is the so-called modified-two-stream instability (MTSI). The MTSI has a frequency close to the lower hybrid resonance, but has a polarization somewhat different from the LHDI (see, for instance, *Gladd* [1975]). We have not pursued the MTSI as an explanation for the wake generated noise for two reasons: firstly, as shown by *Gladd* [1975], in low-beta plasmas with density gradients, the maximum growth rate of the LHDI exceeds that of the MTSI, and secondly, it is unclear whether the MTSI can propagate in the surrounding plasma once it leaves the wake region. It is possible that the MTSI may play a role in the generation of lower hybrid waves in the far downstream region of the wake, where the plasma density gradients are small.

Apart from the ambipolar electric field, another source of the electric field can be attributed to the plasma motion. Because of the large size of the spacecraft, the $\vec{V}_{s/c} \times \vec{B}$ electric field can cause significant plasma potential differences across the bus shield. These potential differences, which can be as much as several volts, are substantially greater than the streaming energy of the plasma. The resulting asymmetry in the fringing fields around the edge of the bus shield could alter the direction of the plasma flow in the downstream wake region. This asymmetry would be along the $\vec{V}_{s/c} \times \vec{B}$ axis. Previous studies of spacecraft wakes by *Stone et al.* [1983] and others have suggested that variations in the plasma potential across

large structures due to the $\vec{V}_{s/c} \times \vec{B}$ electric field may have important effects on the downstream wake structure. In contrast with the ambipolar electric field, which are symmetrical on both sides of the wake, the fringing fields are asymmetric and favor one side.

Although the above linear stability calculation explains the main features of wake-generated noise, there are two features that are not explained. First, from Figure 11, one can see that the bursts near $\phi \sim 15^\circ$ after closest approach have a periodic intensity variation with a period of about two minutes (see Figure 11). Since δ_{wake} increases smoothly throughout this period, the cause of this periodicity remains unknown. Second, as discussed earlier, the spin modulation analysis shows that the waves are primarily generated on the $-\vec{V}_{s/c} \times \vec{B}$ side of the wake. Whether the LHDI model can account for this observed asymmetry depends on a firm identification of the electric field that dominates v_E . If the electric field is dominantly ambipolar, then the theory cannot explain the observed asymmetry. On the other hand, if the electric field is dominated by asymmetric fringing fields, then it can possibly account for the observed asymmetry. In the absence of direct electric field measurements, we are unable to settle this issue unequivocally.

The Doppler Shift

The Galileo spacecraft, at the time of the first Earth flyby, was travelling at a speed between 11 and 14 km/s with respect to the plasmaspheric plasma. Since the growth rate calculations are performed in the plasma rest frame and the measurements were made in the spacecraft frame of reference, the Doppler shift to the observed frequencies must also be taken into account to justify any conclusions

we may make about the type of wave we are observing. The Doppler shift is given by $\Delta f = \frac{\vec{V}_{s/c} \cdot \vec{k}}{2\pi} = (V_{s/c}/\lambda) \cos \phi$, where λ is the wavelength and ϕ is the angle between the wave vector \vec{k} and the spacecraft velocity vector $\vec{V}_{s/c}$. Since $V_{s/c} \simeq 11 - 14$ km/s and $\lambda \simeq 1$ to 5 m during the flyby, the Doppler shift can be substantial, $\Delta f \simeq 2$ to 14 kHz. The large Doppler shift may account for the broad bandwidth of the once-per-rotation bursts. The main difficulty in evaluating the Doppler shift is the $\cos \phi$ factor. The conical configuration of the wake and the associated refraction effects are likely to cause significant variations in the wave vector direction as the wave grows and finally escapes from the wake cavity. Unfortunately, to fully investigate the effects of the changes in the wave vector direction due to the presence of the wake cavity requires detailed ray-tracing calculations and particle simulations. Because of the lack of a detailed density profile throughout the region of the wake cavity, such a detailed level of analysis has not been attempted. For those waves that immediately escape with unchanged \vec{k} into the plasmaspheric plasma, an estimate can be made of the $\cos \phi$ factor. The mathematical development of this estimate is detailed in Appendix A. A plot of $\cos \phi$ values, calculated from conditions observed or assumed in the study interval, is plotted in Figure 20. The vertical axis displays values of $\cos \phi$ from 0.5 to 1.0, while the horizontal axis plots time from 2014 to 2104 UT. The $\cos \phi$ factors have been plotted for both the cylindrical wake model (dot-dashed line) and the conical wake model (solid line). Applying the $\cos \phi$ factor from the conical wake, one can see that for long (~ 5 m) wavelengths, $\Delta f \simeq 1.2$ to 1.9 kHz, while for short (~ 1 m) wavelengths, $\Delta f \simeq 8.7$ to 13.3 kHz.

Also of major importance to the Doppler shift is the wavelength of the waves

generated in the wake. In the theoretical derivation given above, the wavelength associated with maximum growth rate is determined from $k_y \rho_e \approx 1$. One can calculate from this an approximate wavelength of about 70 cm. In contrast to this, we have estimated from considerations of the wake geometry and antenna response that the wavelength should be in the interval $1 \text{ m} \leq \lambda \leq 5 \text{ m}$. In addition, the antenna response function mentioned by *Fuselier and Gurnett* [1984] suggests that longer wavelengths were more likely to have been detected by the electric antenna than shorter wavelengths. To address this apparent incongruity, we note that during a barium release done by the Active Magnetospheric Particle Tracer Explorers (AMPTE), *Bernhardt et al.* [1987] reported observations of magnetic-field-aligned structure on the surface of the injected plasma. *Bernhardt et al.* suggested that the LHDI could be responsible for the structure, but noted that the wavelength was about a factor of ten larger than would be expected from linear theory. The electrostatic particle simulations of *Sydora et al.* [1983] and *Galvez et al.* [1988] have also demonstrated the formation of a similar, long-wavelength structure. It may well be that the mechanism(s) by which longer-wavelength lower hybrid waves are produced are also present to a lesser extent in this case, resulting in longer wavelengths than was determined by our linear theory, and would resolve the apparent disparity between the wavelength calculated from LHDI theory and that inferred by the antenna geometry.

CHAPTER VI

CONCLUSIONS

In this paper we have described an unusual type of broadband electrostatic noise that was observed by the Galileo plasma wave instrument during the first flyby of the Earth. The spectrum of this noise is strongly enhanced near the lower hybrid resonance frequency and has a very pronounced spin modulation with one peak per spacecraft rotation. This type of a spin modulation is inconsistent with a naturally occurring wave field, and indicates that the waves must be generated in close proximity to the spacecraft. Assuming that the wave energy propagates along the magnetic field lines, as would be expected for electrostatic waves near the lower hybrid resonance frequency, we have been able to show that the once-per-rotation modulation is consistent with a source located in the wake immediately downstream of the spacecraft body. We have also shown that one possible method of generating these waves is via the electrostatic lower-hybrid-drift instability (LHDI). Using representative parameters, the growth rate of the LHDI is found to be sufficiently large for waves to grow to large amplitudes in the time it takes for the plasma to fill the wake. Once generated, the wave energy propagates along the magnetic field to a point where the waves can be detected by the electric field antenna. Since the electric antenna is mounted on a long boom well away from the spacecraft body, the optimum geometry for detecting the waves only occurs once per spacecraft ro-

tation, which explains the once-per-rotation modulation. The angular spread of the peak in the modulation pattern is also shown to be consistent with the estimated diameter of the wake, and shows evidence of the expected conical geometry.

Although the basic features of the once-per-rotation bursts are now understood, there are certain detailed characteristics that require further investigation. The peak in the spin modulation pattern consistently showed an offset of about 10 to 15° toward the $-\vec{V}_{s/c} \times \vec{B}$ side of the wake axis. This offset, which corresponds to a shift of about 2 to 3 meters from the wake axis, suggests an asymmetry either in the geometry of the wake, or in the wave generation mechanism. Although the exact cause of the asymmetry is unknown, we have suggested that fringing fields around the spacecraft body caused by the motional $\vec{V}_{s/c} \times \vec{B}$ electric field may play a role in producing the observed asymmetry. Various features of the emission spectrum also remain poorly understood. For example, discrete narrowband U-shaped emissions are frequently observed at frequencies of a few kHz in synchronism with the spacecraft rotation (see Figure 5 at about 12, 31, and 50 s). Similar narrowband emissions have been observed in some sounding rocket flights, such as the one reported by *Gurnett and Mosier* [1969]. However, neither the narrowband emissions observed by Galileo nor the sounding rocket observations have any known explanation within the context of the LHDI mechanism. These narrowband emissions may well be caused by some other current-driven or antenna-associated instability that has not yet been identified. Furthermore, the Doppler shift may account for part of the broad bandwidth of the once-per-rotation bursts and may be involved in the time evolution of the burst spectrum. However, due to the lack of detailed

particle profiles throughout the wake region, we have not attempted a more detailed analysis of the Doppler effect on the observations.

Since we have made a strong case that lower hybrid waves can be produced in the plasma wake of a moving spacecraft, there are two questions which naturally arise. The first question: could lower hybrid waves observed by other Earth-orbiting spacecraft be caused by wake effects? The specific feature that allowed us to conclude that the waves are generated in the spacecraft wake was the mounting of the electric antenna on a boom well away from the spacecraft body. This mounting configuration resulted in the characteristic once-per-rotation modulation. In most other space plasma wave investigations the electric antennas were usually mounted on the spacecraft body with the elements extending symmetrically outwards in opposite directions. With this type of symmetrical antenna configuration, it is quite difficult to distinguish spacecraft-generated waves from naturally occurring waves, since both give a twice-per-rotation modulation. It is possible that some reports of magnetospherically generated lower hybrid waves may in fact be generated by spacecraft-plasma interactions [for example, see *Gurnett et al.*, 1969]. Since an adequate path length must exist for the waves to grow to large amplitudes, the likelihood of such effects increases as the dimensions of the spacecraft increase.

The second question to naturally arise from this research: is it reasonable to expect once-per-rotation bursts, similar to those reported here, to be observed when Galileo is at Jupiter? This question breaks down into three others: will there be a significant wake region, will the lower hybrid frequency be observable, and will the LHDI mechanism be satisfied? To determine if there will be a significant wake,

consider again the half-angle of the wake cone, $\arctan(v_{ith}/V_{s/c})$. Since Galileo will generally not venture within $10 R_J$ (Jupiter radii) of the planet, the spacecraft speed will be in the range of 13 to 19 km/s. Meanwhile, it can be shown that the speed of the corotating plasma is about 50 km/s [Gurnett, 1971]. Thus, the speed at which plasma passes the spacecraft will generally be in the range of 30 to 40 km/s. The regions of highest plasma density are expected to be in the Io plasma torus, which is composed largely of sulfur ions with an energy of about 40 eV [Frank et al., 1992]. This implies that v_{ith} for the sulfur ions in the torus has a value of just over 10 km/s, and thus $\arctan(v_{ith}/V_{s/c}) \approx 14^\circ$ to 18° , which in turn suggests a wake length of 7 to 9 meters, which is of the same order of magnitude as the wake estimated during the Earth flyby. To detect the resulting lower hybrid waves, we must note that because the Jovian magnetic field is ten times stronger than that of Earth, the lower hybrid resonance frequency will correspondingly be higher as well. Gurnett, Kurth, and Scarf [1979] have shown that the lower hybrid resonance rises to 9 kHz at about $5.6 R_J$, so lower hybrid waves will not be detectable at radial distances inside of about $5.5 R_J$ by the wideband receiver in the 10 kHz mode. However, the lower hybrid resonance frequency should remain well within the range of the step-frequency receiver throughout the region of Jupiter's magnetosphere that the spacecraft will explore. The question of satisfying the requirements of the LHDI mechanism is complicated by the strong Jovian magnetic field, and by the presence and compositions of the Io plasma torus and the disk-like plasma "belt" which serves to significantly distort the magnetic field from a dipolar configuration. To properly evaluate the instability would require numerically re-solving the dispersion relation,

assuming Jovian conditions, and reconstructing Figures 16 through 19 with these results.

Finally, it may be worth pointing out that lower hybrid waves attributed to other sources could be explained by the LHDI mechanism. For example, lower hybrid waves have been reported in the wake of the space shuttle [Murphy *et al.*, 1983; Gurnett *et al.*, 1988; Feng *et al.*, 1993]. These waves have been attributed to interactions involving pick-up ions from the water cloud around the shuttle [Papadopoulos, 1984; Cairns and Gurnett, 1991]. However, given the role that the LHDI may play in the Galileo interaction, it would appear that the LHDI mechanism should be considered as a possible mechanism for generating the waves observed downstream of the shuttle.

REFERENCES

- Allcock, G.McK., *A Study of the Audio-Frequency Radio Phenomenon Known as "Dawn Chorus"*, *Australian J. Phys.*, **10**, 286-98, 1957.
- Barrington, R.E., and Belrose, J.S., *Preliminary Results from the Very-low-frequency Receiver Aboard Canada's Alouette Satellite*, *Nature*, **198**, 651-6, 1963.
- Bauer, S.J. and Stone, R.G., *Satellite Observations of Radio Noise in the Magnetosphere*, *Nature*, **218**, 1145-7, 1968.
- Brice, N.M., and Smith, R.L., *Lower Hybrid Resonance Emissions*, *J. Geophys. Res.*, **70**, 71-80, 1965.
- Cairns, I.H. and Gurnett, D.A., *Control of Plasma Waves Associated with the Space Shuttle by the Angle Between the Orbiter's Velocity Vector and the Magnetic Field*, *J. Geophys. Res.*, **96**, 7591-601, 1991.
- Carpenter, D.L., *Whistler Studies of the Plasmapause in the Magnetosphere. 1. Temporal Variations in the Position of the Knee and Some Evidence on Plasma Motions near the Knee*, *J. Geophys. Res.*, **71**, 693-709, 1966.
- Carpenter, D.L., *Whistler Evidence of a "Knee" in the Magnetospheric Ionization Density Profile*, *J. Geophys. Res.*, **68**, 1675-82, 1963.
- Davidson, R.C., Gladd, N.T., Huba, J., Hui, B.H., Liewer, P.C., Liu, C.S., Mondt, J.P., Ogden, J.M., Wu, C.S., Hamasaki, S., Krall, N.A., and Wagner, C.E., *Kinetic and Numerical Studies of Microstability Properties and Anomalous Transport in Theta Pinches*, *Nucl. Fusion (Australia)*, Suppl. **3**, 113-20, 1977.
- Feng, W., Gurnett, D.A., and Cairns, I.H., *Interference Patterns in the Spacelab 2 Plasma Wave Data: Lower Hybrid Waves Driven by Pickup Ions*, *J. Geophys. Res.*, **98**, 21571-80, 1993.
- Frank, L.A., Ackerson, K.L., Lee, J.A., English, M.R., and Pickett, G.L., *The Plasma Instrumentation for the Galileo Mission*, *Space Sci. Rev.*, **60**, 283-307, 1992.

- Fuselier, S.A., and Gurnett, D.A., *Short Wavelength Ion Waves Upstream of the Earth's Bow Shock*, *J. Geophys. Res.*, **89**, 91-103, 1984.
- Gladd, N.T., *The Lower Hybrid Drift Instability and the Modified Two Stream Instability in High Density Theta Pinch Environments*, *Plasma Phys. (GB)*, **18**, 27-40, 1976.
- Gregory, P.C., *Radio Emission from Auroral Electrons*, *Nature*, **221**, 350-2, 1969.
- Gurnett, D.A., *Sheath Effects and Related Charged-particle Acceleration by Jupiter's Satellite Io*, *Astrophys. J.*, **175**, 525-33, 1971.
- Gurnett, D.A., Kurth, W.S., and Scarf, F.L., *Auroral Hiss Observed Near the Io Plasma Torus*, *Nature*, **280**, 767-70, 1979.
- Gurnett, D.A., Kurth, W.S., Shaw, R.R., Roux, A., Gendrin, R., Kennel, C.F., Scarf, F.L., and Shawhan, S.D., *The Galileo Plasma Wave Investigation*, *Space Sci. Rev.*, **60**, 341-55, 1992.
- Gurnett, D.A., Kurth, W.S., and Steinberg, J.T., *Plasma Turbulence Around the Shuttle: Results from the Spaceleab-2 Flight*, *Geophys. Res. Lett.*, **15**, 760-3, 1988.
- Gurnett, D.A., and Mosier, S.R., *VLF Electric and Magnetic Fields Observed in the Auroral Zone with the Javelin 8.46 Sounding Rocket*, *J. Geophys. Res.*, **74**, 3979-91, 1969.
- Gurnett, D.A., Pfeiffer, G.W., Anderson, R.R., Mosier, S.R., and Cauffman, D.P., *Initial Observations of VLF Electric and Magnetic Fields with the Injun 5 Satellite* *J. Geophys. Res.*, **74**, 4631, 1969.
- Hartz, T.R., *Radio Noise Levels Within and Above the Ionosphere*, *Proc. I. E. E.*, **57**, 1042, 1969.
- Katz, I., D.E. Parks, and Wright, Jr., K.H., *A Model of a Plasma Wake Generated by a Large Object*, *IEEE Trans. Nucl. Sci.*, NS-32, 4092, 1985.
- Krall, N.A., *Shear Stabilization of Lower Hybrid Drift Instabilities*, *Phys. Fluids*, **20**, 311-2, 1977.
- Krall, N.A., and Liewer, P.C., *Low-frequency Instabilities in Magnetic Pulses*, *Phys. Rev. A*, **4**, 2094-103, 1971.

- McEwen, D.J., and Barrington, R.E., *Some Characteristics of the Lower Hybrid Resonance Noise Bands Observed by the Alouette 1 Satellite*, *Can. J. Phys.*, **45**, 13, 1967.
- Mosier, S.R., and Gurnett, D.A., *VLF Measurements of the Poynting Flux Along the Geomagnetic Field with the Injun 5 Satellite*, *J. Geophys. Res.*, **74**, 5675-87, 1969.
- Mosier, S.R., Kaiser, M.L., and Brown, L.W., *Observations of Noise Bands Associated with the Upper Hybrid Resonance by the IMP 6 Radio Astronomy Experiment*, *J. Geophys. Res.*, **78**, 1673-80, 1973.
- Murphy, G.B., Shawhan, S.D., Frank, L.A., D'Angelo, N., Gurnett, D.A., Grebowsky, J.M., Reasoner, D.L., and Stone, N., *Interaction of the Space Shuttle Orbiter with the Ionospheric Plasma, Spacecraft/Plasma Interactions and Their Influence on Field and Particle Measurements*, *Eur. Space Agency Spec. Publ.*, **ESA SP-198**, 73, 1983.
- Papadopoulos, K.D., *On the Shuttle Glow (the Plasma Alternative)*, *Radio Sci.*, **19**, 571, 1984.
- Parady, B.K., and Cahill, L.J., *ELF Observations During the December 1971 Storm*, *J. Geophys. Res.*, **78**, 4765, 1973.
- Russell, C.T., Holzer, R.E., and Smith, E.J., *Observations of ELF Noise in the Magnetosphere I: Spatial Extent and Frequency of Occurrence*, *J. Geophys. Res.*, **74**, 755-77, 1969.
- Stix, T.H., *The Theory of Plasma Waves*, McGraw-Hill, N. York, 10, 1962.
- Stone, N.H., Wright, K.H., Jr., Samir, U., and Hwang, K.S., *On the Expansion of Ionospheric Plasma into the Near-Wake of the Space Shuttle Orbiter*, *Geophys. Res. Lett.*, **15**, 1169-72, 1988.
- Storey, L.R.O., *An Investigation of Whistling Atmospherics*, *Phil. Trans A*, **246**, 113, 1953.
- Storey, L.R.O., and Cerisier, J.-C., *An Interpretation of the Noise Bands Observed Near the Lower Hybrid Resonance Frequency by Artificial Satellites*, *C.R. Acad. Sc. Paris*, **266**, 525-8, 1968.
- Thorne, R.M., Smith, E.J., Burton, R.K., and Holzer, R.E., *Plasmaspheric Hiss*, *J. Geophys. Res.*, **78**, 1581, 1973.

- Walsh, D., Haddock, F.T., and Schulte, H.F., *Cosmic Radio Intensities at 1.225 and 2.0 Mc Measured up to an Altitude of 1700 km*, in *Space Research*, vol. 4, ed. P. Muller, p. 935, 1964, North Holland, Amsterdam, The Netherlands
- Yoon, P.H., Lui, A.T.Y., and Chang, C.-L., *Lower-Hybrid-Drift Instability Operative in the Geomagnetic Tail*, *Plasma Phys. (USA)*, 1(9), 3033, 1994.

APPENDIX A

ESTIMATION OF THE $\cos \phi$ FACTOR

In doing this problem, the most effective approach is to solve for the case of the conical wake model, for then the cylindrical wake model can easily be checked by setting the ion thermal velocity, v_{ith} , to zero. Recall that

$$\Delta f = \frac{\vec{V}_{s/c} \cdot \vec{k}}{2\pi} = \left(\frac{V_{s/c}}{\lambda} \right) \cos \phi,$$

where λ is the wavelength and ϕ is the angle between the wave vector \vec{k} and the spacecraft velocity vector $\vec{V}_{s/c}$. To correctly define the boundary of the wake model, a suitable coordinate system must be chosen. Since both wake models depend upon $\vec{V}_{s/c}$, we first take $\hat{V}_{s/c} = \frac{\vec{V}_{s/c}}{V_{s/c}}$ as one of the unit vectors for this coordinate system. Since

$$\vec{E} = -\vec{V}_{s/c} \times \vec{B}$$

is perpendicular to $\vec{V}_{s/c}$, we will choose the unit vector in this direction (\hat{E}) as the one orthogonal unit vector in the plane perpendicular to $\vec{V}_{s/c}$. For the other orthogonal unit vector, we choose the unit normal of the vector defined by

$$\vec{N} = \vec{V}_{s/c} \times \vec{E},$$

and denoted by \hat{N} . By defining θ as the angle measured counterclockwise from \hat{E} to

the position vector in the $\hat{E} - \hat{N}$ plane centered around where $\vec{V}_{s/c}$ passes through the center of the bus shield, the conical wake edge can be approximately defined by the initial points around the edge of the bus shield

$$\vec{P}_i(\theta) = S_r(\hat{E} \cos \theta + \hat{N} \sin \theta)$$

and the corresponding edge lines

$$\vec{W}_i(\theta) = -\vec{V}_{s/c} - v_{ith}(\hat{E} \cos \theta + \hat{N} \sin \theta)$$

where S_r is the bus shield radius (2.1 m), and $v_{ith} \approx 4.8$ km/s.

From LHDI theory, note that \hat{x} must be perpendicular to the local edge of the wake, so since $\vec{V}_{s/c} \times \vec{W}_i$ is perpendicular to the plane containing both $\vec{V}_{s/c}$ and \vec{W}_i (and the wake, in this plane, appears as in Fig. 12b), it is easy to see that $\vec{V}_{s/c} \times \vec{W}_i$ is tangent to the wake cone along \vec{W}_i . The inward perpendicular is given by $\vec{W}_i \times (\vec{V}_{s/c} \times \vec{W}_i)$. Therefore,

$$\hat{x} = \frac{\vec{W}_i \times (\vec{V}_{s/c} \times \vec{W}_i)}{|\vec{W}_i \times (\vec{V}_{s/c} \times \vec{W}_i)|}.$$

We have shown that LHDI gives us $\vec{k} \approx k\hat{y}$, where $\vec{B} \perp \hat{y} \perp \hat{x}$. Thus,

$$\hat{y} = \frac{\vec{B} \times \hat{x}}{|\vec{B} \times \hat{x}|}.$$

One begins by evaluating $\vec{W}_i \times (\vec{V}_{s/c} \times \vec{W}_i)$:

$$\begin{aligned}
\vec{W}_i \times (\vec{V}_{s/c} \times \vec{W}_i) &= W_i^2 \vec{V}_{s/c} - (\vec{W}_i \cdot \vec{V}_{s/c}) \vec{W}_i \\
&= (V_{s/c}^2 + v_{ith}^2) \vec{V}_{s/c} - (-V_{s/c}^2) [-\vec{V}_{s/c} - v_{ith}(\hat{E} \cos \theta + \hat{N} \sin \theta)] \\
&= v_{ith}^2 \vec{V}_{s/c} - v_{ith} V_{s/c}^2 (\hat{E} \cos \theta + \hat{N} \sin \theta),
\end{aligned}$$

and since $\vec{V}_{s/c} \perp \hat{E} \perp \hat{N}$,

$$\begin{aligned}
|\vec{W}_i \times (\vec{V}_{s/c} \times \vec{W}_i)| &= \sqrt{v_{ith}^4 V_{s/c}^2 + V_{s/c}^4 v_{ith}^2 (\cos^2 \theta + \sin^2 \theta)} \\
&= v_{ith} V_{s/c} \sqrt{V_{s/c}^2 + v_{ith}^2},
\end{aligned}$$

so

$$\hat{x} = \left(\frac{v_{ith}}{V_{s/c} \sqrt{V_{s/c}^2 + v_{ith}^2}} \right) \vec{V}_{s/c} - \left(\frac{V_{s/c}}{V_{s/c} \sqrt{V_{s/c}^2 + v_{ith}^2}} \right) [\hat{E} \cos \theta + \hat{N} \sin \theta].$$

The cosine factor being sought is related to \hat{y} by the following:

$$k \vec{V}_{s/c} \cdot \hat{y} = \vec{V}_{s/c} \cdot \vec{k} = k V_{s/c} \cos \phi,$$

so

$$\frac{\vec{V}_{s/c} \cdot \hat{y}}{V_{s/c}} = \cos \phi.$$

Assuming that no significant change of \vec{k} occurs as the waves escape from the wake, we have

$$\hat{y} = \frac{\vec{B} \times \hat{x}}{|\vec{B} \times \hat{x}|}.$$

First evaluating $\vec{B} \times \hat{x}$:

$$\begin{aligned}\vec{B} \times \hat{x} &= \left(\frac{v_{ith}}{V_{s/c} \sqrt{V_{s/c}^2 + v_{ith}^2}} \right) [\vec{B} \times \vec{V}_{s/c}] \\ &\quad - \left(\frac{V_{s/c}}{V_{s/c} \sqrt{V_{s/c}^2 + v_{ith}^2}} \right) [(\vec{B} \times \hat{E}) \cos \theta + (\vec{B} \times \hat{N}) \sin \theta].\end{aligned}$$

Since $\vec{B} \perp \hat{E}$, one can write

$$\begin{aligned}\vec{B} &= (B \cos \Theta) \hat{V}_{s/c} + (B \sin \Theta) \hat{N} \\ &= \left(\frac{\vec{B} \cdot \vec{V}_{s/c}}{V_{s/c}} \right) \frac{\vec{V}_{s/c}}{V_{s/c}} + \left(\frac{|\vec{B} \times \vec{V}_{s/c}|}{V_{s/c}} \right) \hat{N} \\ &= \left(\frac{\vec{B} \cdot \vec{V}_{s/c}}{V_{s/c}^2} \right) \vec{V}_{s/c} + \left(\frac{E}{V_{s/c}} \right) \hat{N}\end{aligned}$$

where Θ is the angle between \vec{B} and $\vec{V}_{s/c}$. Thus,

$$\vec{B} \times \hat{N} = - \left(\frac{\vec{B} \cdot \vec{V}_{s/c}}{V_{s/c}} \right) \hat{E},$$

and

$$\begin{aligned}\vec{B} \times \hat{E} &= \left(\frac{\vec{B} \cdot \vec{V}_{s/c}}{V_{s/c}^2} \right) [V_{s/c} \hat{N}] - \left(\frac{E}{V_{s/c}} \right) \hat{V}_{s/c} \\ &= \left(\frac{E}{V_{s/c}} \right) \hat{N} - \left(\frac{|\vec{B} \times \vec{V}_{s/c}|}{V_{s/c}^2} \right) \vec{V}_{s/c}.\end{aligned}$$

Therefore,

$$\begin{aligned}
\vec{B} \times \hat{x} &= \left(\frac{v_{ith}}{V_{s/c} \sqrt{V_{s/c}^2 + v_{ith}^2}} \right) \vec{E} \\
&\quad - \left(\frac{V_{s/c}}{\sqrt{V_{s/c}^2 + v_{ith}^2}} \right) \left[\left(\frac{\vec{B} \cdot \vec{V}_{s/c}}{V_{s/c}} \right) \hat{N} - \left(\frac{E}{V_{s/c}^2} \right) \vec{V}_{s/c} \right] \cos \theta \\
&\quad - \left(\frac{V_{s/c}}{\sqrt{V_{s/c}^2 + v_{ith}^2}} \right) \left[- \left(\frac{\vec{B} \cdot \vec{V}_{s/c}}{V_{s/c}} \right) \hat{E} \right] \sin \theta \\
&= \left(\frac{E \cos \theta}{V_{s/c} \sqrt{V_{s/c}^2 + v_{ith}^2}} \right) \vec{V}_{s/c} + \left(\frac{v_{ith} E}{V_{s/c} \sqrt{V_{s/c}^2 + v_{ith}^2}} + \frac{(\vec{B} \cdot \vec{V}_{s/c}) \sin \theta}{\sqrt{V_{s/c}^2 + v_{ith}^2}} \right) \hat{E} \\
&\quad - \left(\frac{(\vec{B} \cdot \vec{V}_{s/c}) \cos \theta}{\sqrt{V_{s/c}^2 + v_{ith}^2}} \right) \hat{N}.
\end{aligned}$$

The length of this vector is

$$\begin{aligned}
|\vec{B} \times \hat{x}|^2 &= \frac{E^2 V_{s/c}^2 \cos^2 \theta}{V_{s/c}^2 (V_{s/c}^2 + v_{ith}^2)} + \frac{[v_{ith} E + V_{s/c} (\vec{B} \cdot \vec{V}_{s/c}) \sin \theta]^2}{V_{s/c}^2 (V_{s/c}^2 + v_{ith}^2)} + \frac{(\vec{B} \cdot \vec{V}_{s/c})^2 \cos^2 \theta}{(V_{s/c}^2 + v_{ith}^2)} \\
&= \frac{V_{s/c}^2 E^2 \cos^2 \theta + v_{ith}^2 E^2}{V_{s/c}^2 (V_{s/c}^2 + v_{ith}^2)} \\
&\quad + \frac{2V_{s/c} v_{ith} E (\vec{B} \cdot \vec{V}_{s/c}) \sin \theta + V_{s/c}^2 (\vec{B} \cdot \vec{V}_{s/c})^2 [\cos^2 \theta + \sin^2 \theta]}{V_{s/c}^2 (V_{s/c}^2 + v_{ith}^2)} \\
&= \frac{(V_{s/c}^2 E^2 + v_{ith}^2 E^2) \cos^2 \theta}{V_{s/c}^2 (V_{s/c}^2 + v_{ith}^2)} \\
&\quad + \frac{v_{ith}^2 E^2 \sin^2 \theta + 2V_{s/c} v_{ith} E (\vec{B} \cdot \vec{V}_{s/c}) \sin \theta + V_{s/c}^2 (\vec{B} \cdot \vec{V}_{s/c})^2}{V_{s/c}^2 (V_{s/c}^2 + v_{ith}^2)},
\end{aligned}$$

thus

$$|\vec{B} \times \hat{x}| = \frac{\sqrt{(V_{s/c}^2 + v_{ith}^2)E^2 \cos^2 \theta + [v_{ith}E \sin \theta + V_{s/c}(\vec{B} \cdot \vec{V}_{s/c})]^2}}{V_{s/c}\sqrt{V_{s/c}^2 + v_{ith}^2}}.$$

Recall that

$$\frac{\vec{V}_{s/c} \cdot \hat{y}}{V_{s/c}} = \frac{\vec{V}_{s/c} \cdot (\vec{B} \times \hat{x})}{V_{s/c} |\vec{B} \times \hat{x}|} = \cos \phi.$$

By substituting for \hat{y} in this equation and doing the dot product, one finds

$$\begin{aligned} \cos \phi &= \frac{\frac{V_{s/c}^2 E \cos \theta}{V_{s/c} \sqrt{V_{s/c}^2 + v_{ith}^2}} \cdot V_{s/c} \sqrt{V_{s/c}^2 + v_{ith}^2}}{\sqrt{(V_{s/c}^2 + v_{ith}^2)E^2 \cos^2 \theta + [v_{ith}E \sin \theta + V_{s/c}(\vec{B} \cdot \vec{V}_{s/c})]^2}} \\ &= \frac{EV_{s/c} \cos \theta}{\sqrt{(V_{s/c}^2 + v_{ith}^2)E^2 \cos^2 \theta + [v_{ith}E \sin \theta + V_{s/c}(\vec{B} \cdot \vec{V}_{s/c})]^2}}. \end{aligned}$$

One must remember that this derivation does not take into account any effects of wave reflection or refraction caused by the changing index of refraction at the edges of the wake cavity. In examining the magnetic field and spacecraft velocity vectors throughout the flyby, it was found that the angle between them ranged over the interval $42^\circ < \Theta < 137^\circ$. In addition, at $\theta = n\pi$ (where $n = 0$ or 1), the local normal to the surface of the cylindrical wake, \hat{x} , is parallel to the \hat{E} vector. Thus, when $\Theta = 90^\circ$ and $\theta = n\pi$, the local \hat{y} of the cylindrical wake should lie parallel to $\vec{V}_{s/c}$, maximizing the value of $\cos \phi$. Therefore, we evaluated the $\cos \phi$ equation at $\theta = 0$, using measurements obtained from this flyby or assumed from observations taken by other satellites.

APPENDIX B. FIGURES

Figure 1. The Galileo Earth-1 flyby trajectory, in Geocentric Solar Magnetospheric (GSM) coordinates, projected onto the $x - y$ plane in the top panel and the $x - z$ plane in the bottom panel. The scale is in Earth radii (R_E), and the Earth is represented by the half-shaded circle. Universal Time (UT) is indicated at one-hour intervals along the trajectory.

A-G95-107

GALILEO'S GSM POSITION DURING EARTH-I FLYBY

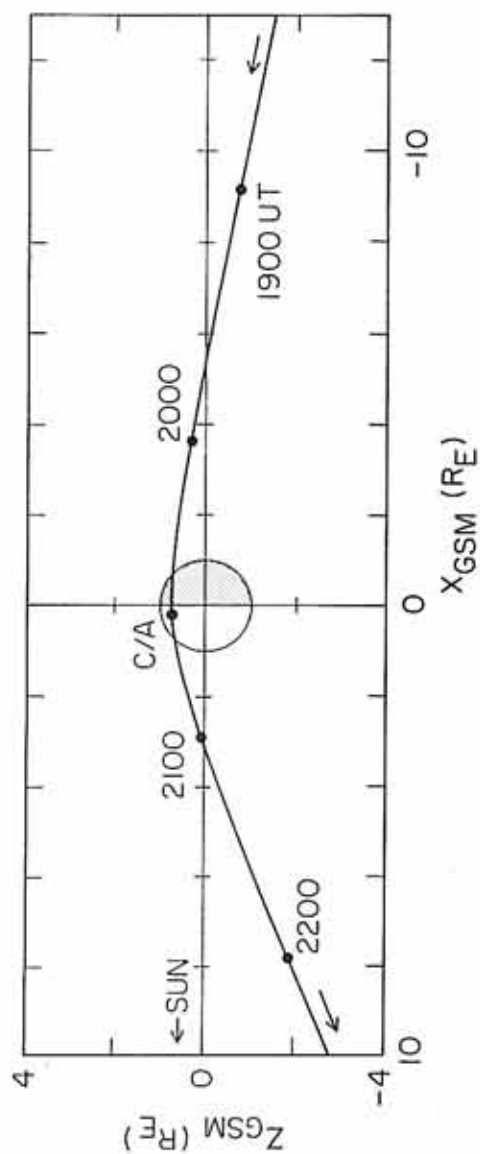
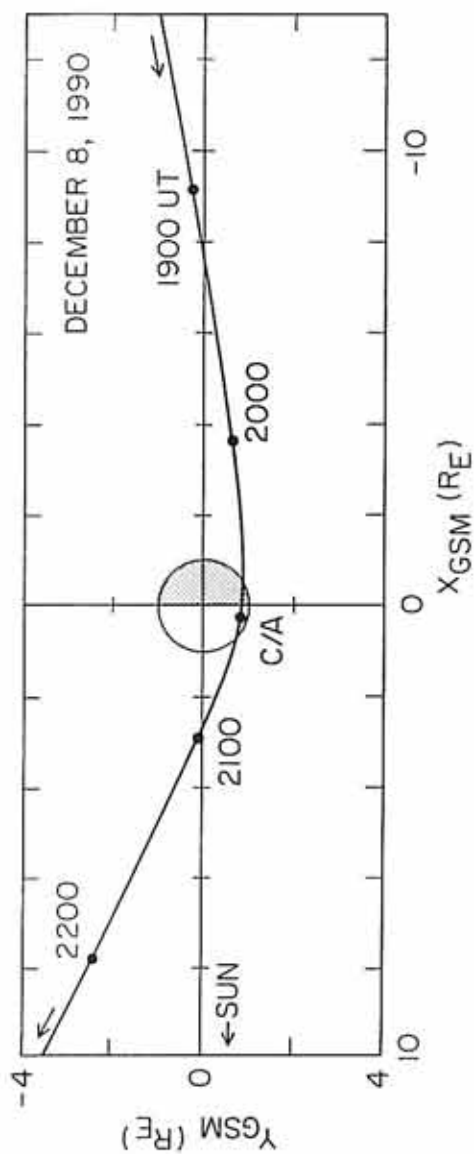


Figure 2. A drawing of the Galileo spacecraft, showing the locations of the electric dipole at the end of the 10.6-meter boom, the magnetic search coil antenna, the bus shield, and the Radioisotope Thermoelectric Generators (RTGs). The spacecraft rotates about the vertical line labelled "spin axis."

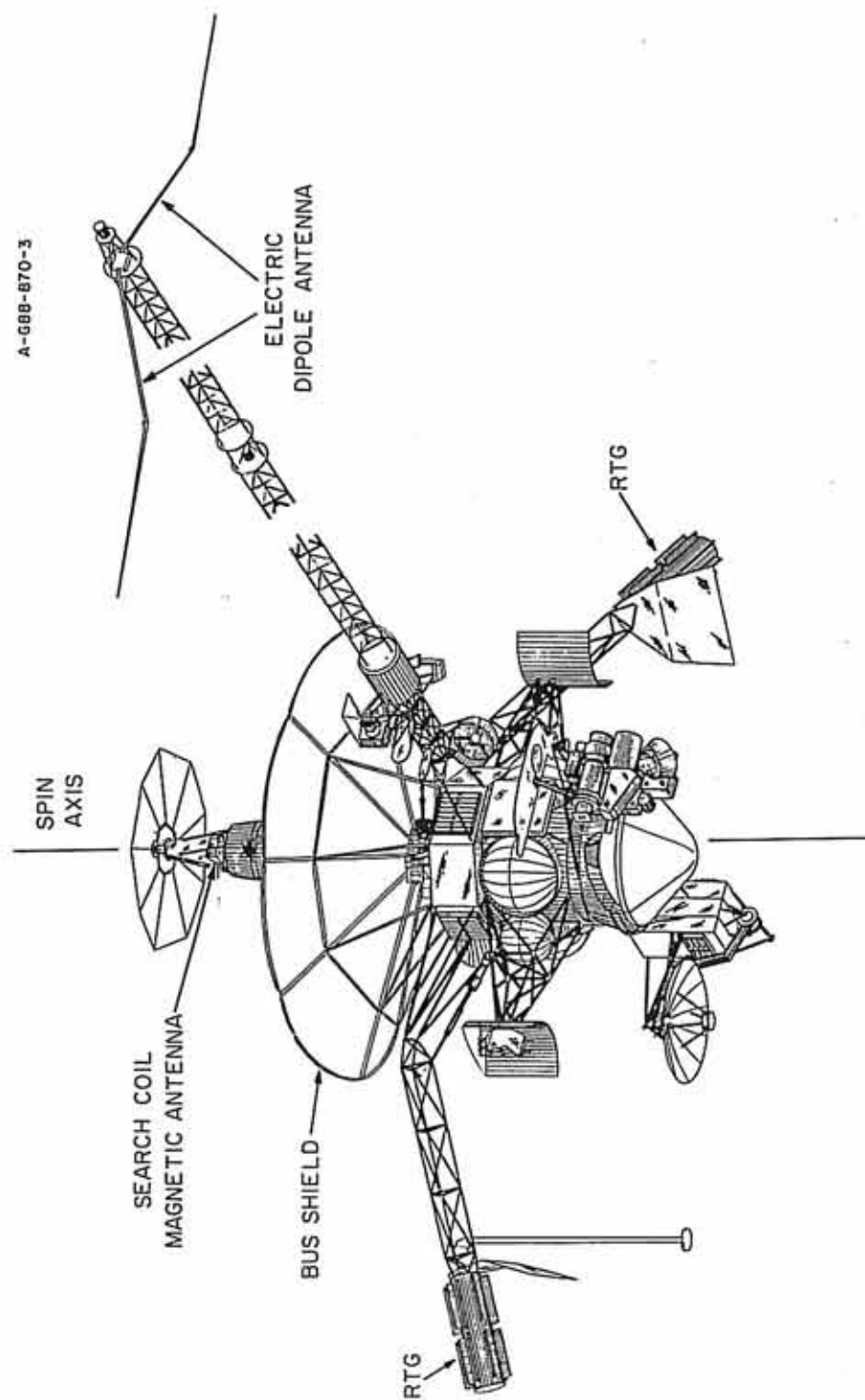


Figure 3. A diagram showing the scheme for sampling the outputs from the medium-frequency spectrum analyzer channels. The frequency channels are grouped into four bands. The basic sampling cycle is completed in 28 steps, which corresponds to a time interval of 18.67 s [adapted from *Gurnett et al.*, 1992].

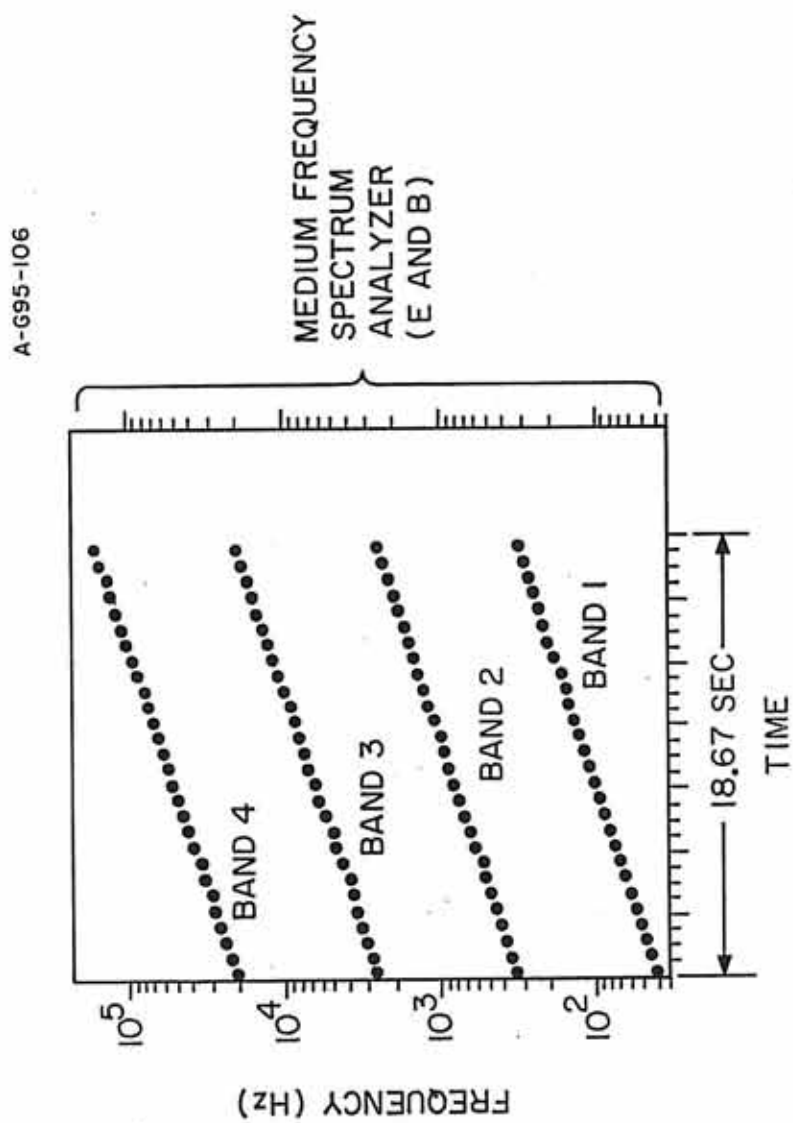
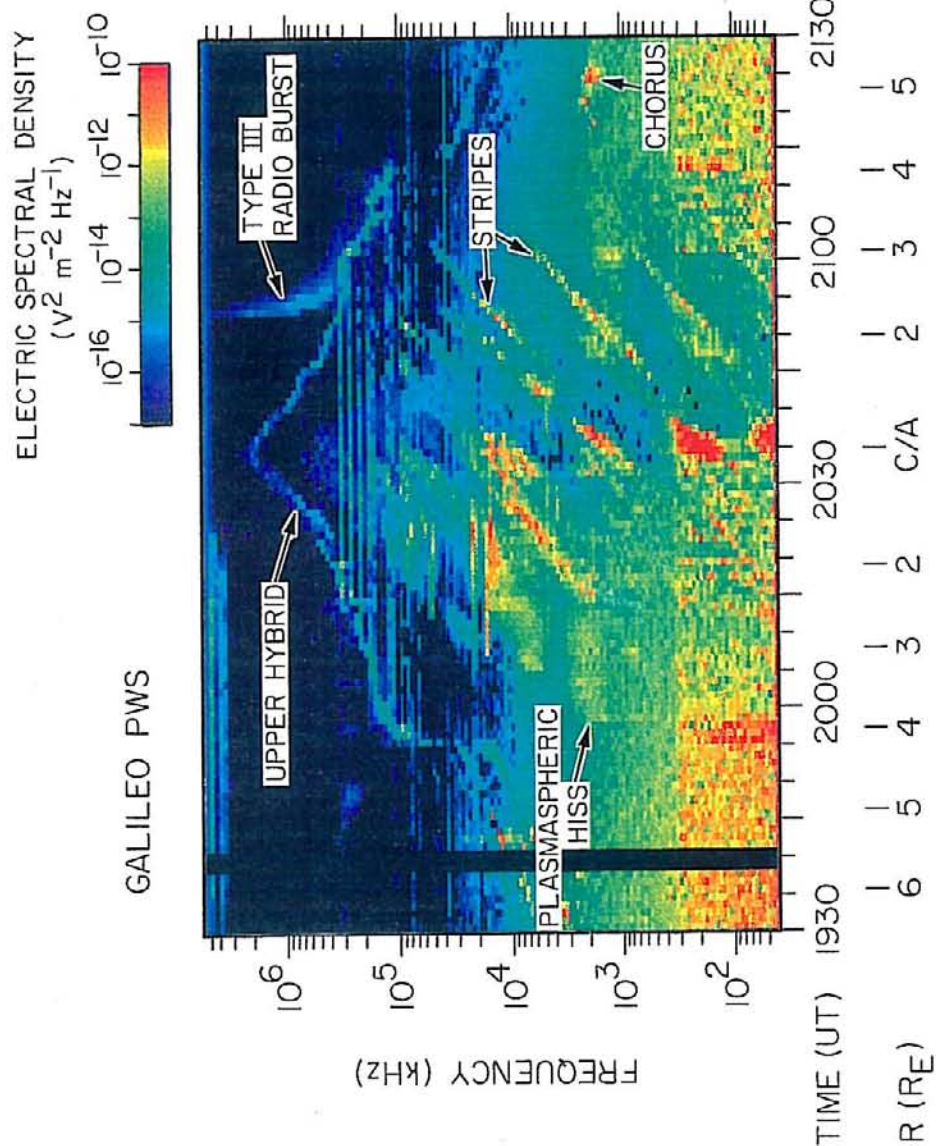


Figure 4. A frequency-time spectrogram of wave electric spectral density from the step-frequency receiver during the Earth-1 flyby. The vertical axis shows the frequency in Hertz (Hz) and the horizontal axis shows Universal Time (UT). Color indicates electric spectral density from 10^{-17} (blue) to 10^{-10} (red) $\text{V}^2 \text{m}^{-2} \text{Hz}^{-1}$.

A-695-124-2



DAY 342, DECEMBER 8, 1990

Figure 5. A wideband frequency-time spectrogram taken well before closest approach. The vertical axis shows frequency in kiloHertz (kHz) and the horizontal axis shows time, called relative time, in seconds after 2016:16 UT. The relative wave electric spectral density is shown in color on a scale from 0 (blue) to 40 (red) dB. The lower hybrid resonance frequency is indicated by a white line labelled f_{LHR} .

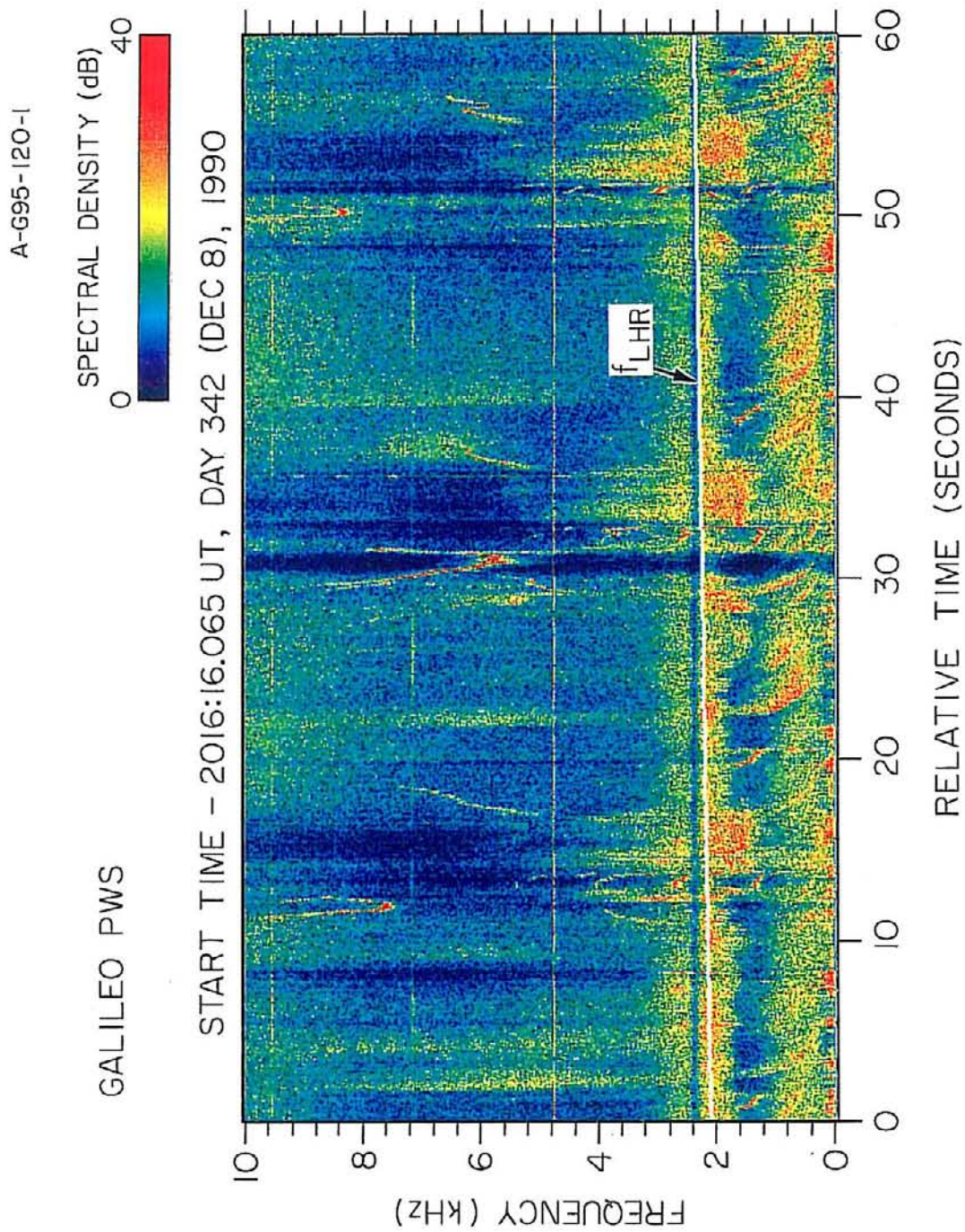


Figure 6. A wideband frequency-time spectrogram density taken shortly after closest approach, displayed in a format exactly similar to Fig. 5. This spectrogram shows a series of clearly defined, once-per-spin bursts near the lower hybrid resonance frequency, f_{LHR} . The horizontal lines are interference at harmonics of the spacecraft power system, which operates at a frequency of 2.4 kHz.

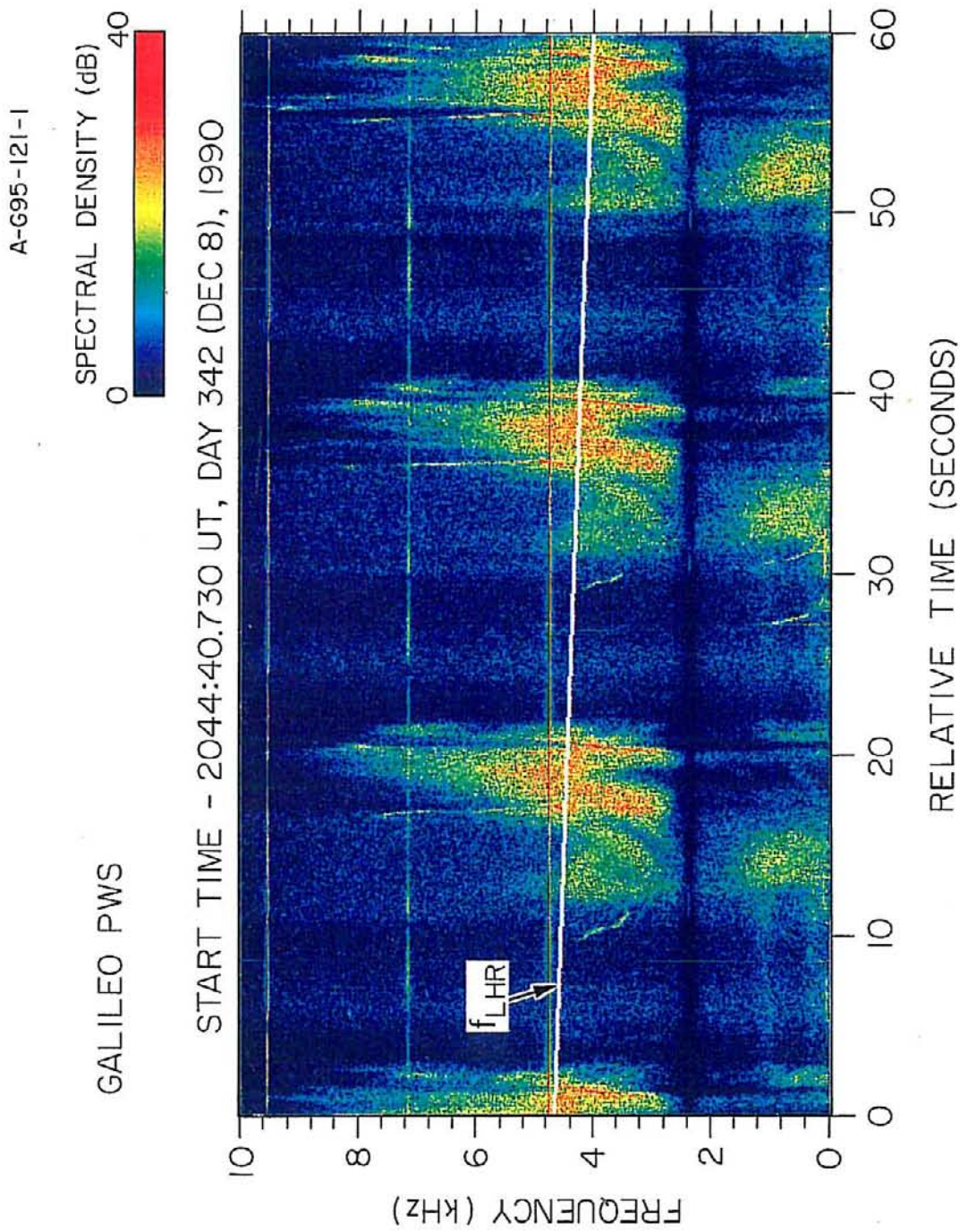


Figure 7. A wideband frequency-time spectrogram taken well after closest approach in a format exactly similar to Fig. 5. Note that the frequency scale is now 0-80 kHz. This spectrogram shows a series of broadband once-per-spin bursts extending over the entire frequency range. The spectrum of these bursts shows a strong intensification near the lower hybrid resonance frequency, f_{LHR} , which is near the bottom of the spectrogram (white line).

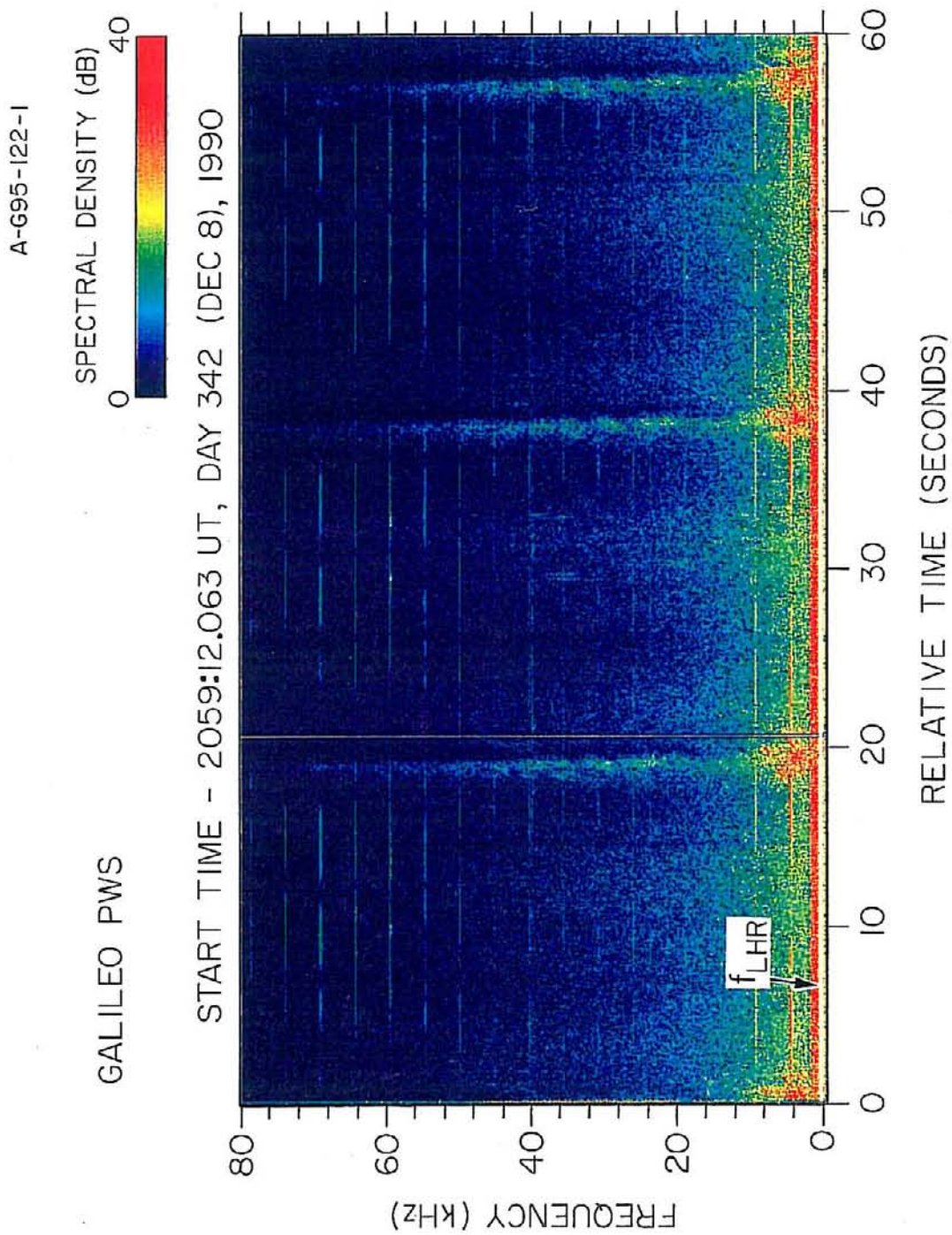


Figure 8. A wideband frequency-time spectrogram similar to Figures 5, 6, and 7, but with the time scale compressed to show all of the wideband measurements taken in the region around closest approach, from 2014 UT to 2104 UT. The once-per-spin bursts appear as a series of closely spaced vertical spikes. The spectrum of these spikes has a clearly defined enhancement near the lower hybrid resonance frequency, f_{LHR} , which is shown by the white line.

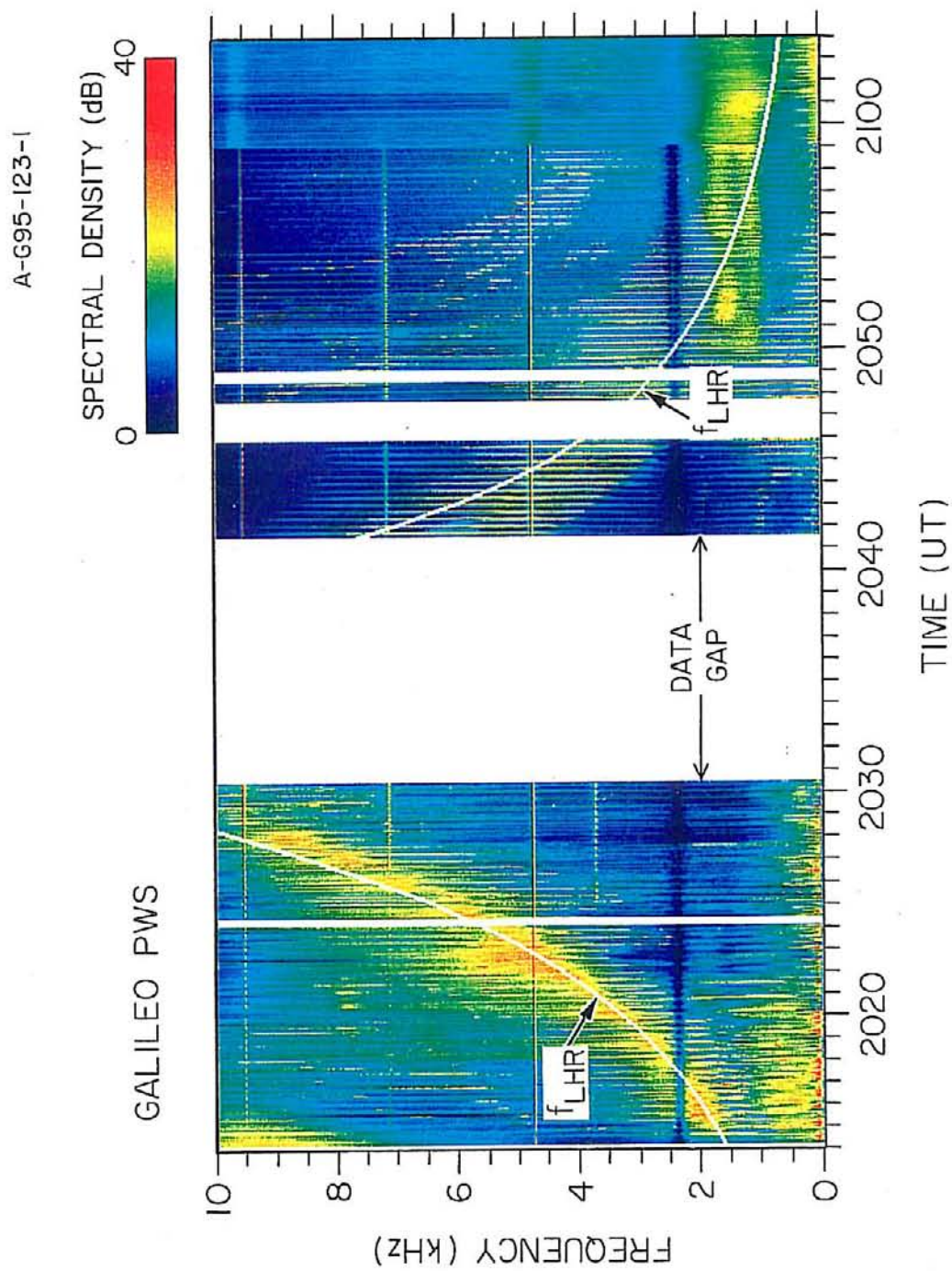


Figure 9. A sketch of a magnetic field line linking Galileo's electric antenna to the spacecraft's wake. The spacecraft motion is right to left and out of the paper, and spins clockwise from this viewpoint. The point marked is the intersection of the magnetic field line and the wake axis. Waves leaving the wake along the magnetic field line pass through the antenna and are detected as electric waves or noise.

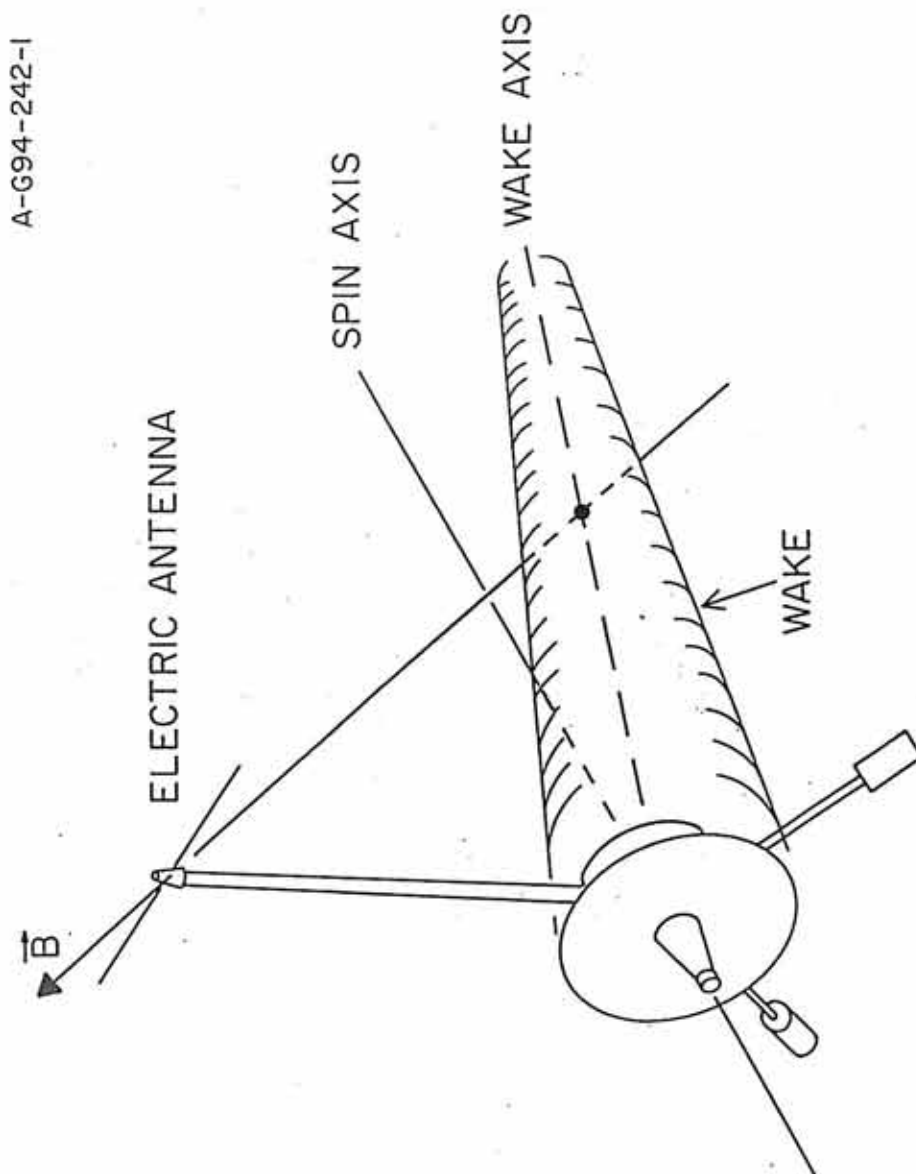


Figure 10. Two views, looking parallel and perpendicular to the spin axis, showing the geometry at the time that the magnetic field line through the antenna intersects the wake axis. The rotation angle ϕ is defined as the angle between the electric antenna boom and the projection of the magnetic field onto the spin plane, \vec{B}_\perp . At the time of intersection, $\phi = \phi_{wake}$. The parameter δ_{wake} is the distance from the center of the spacecraft body to the intersection of the magnetic field line and the wake axis.

A-G95-72-1

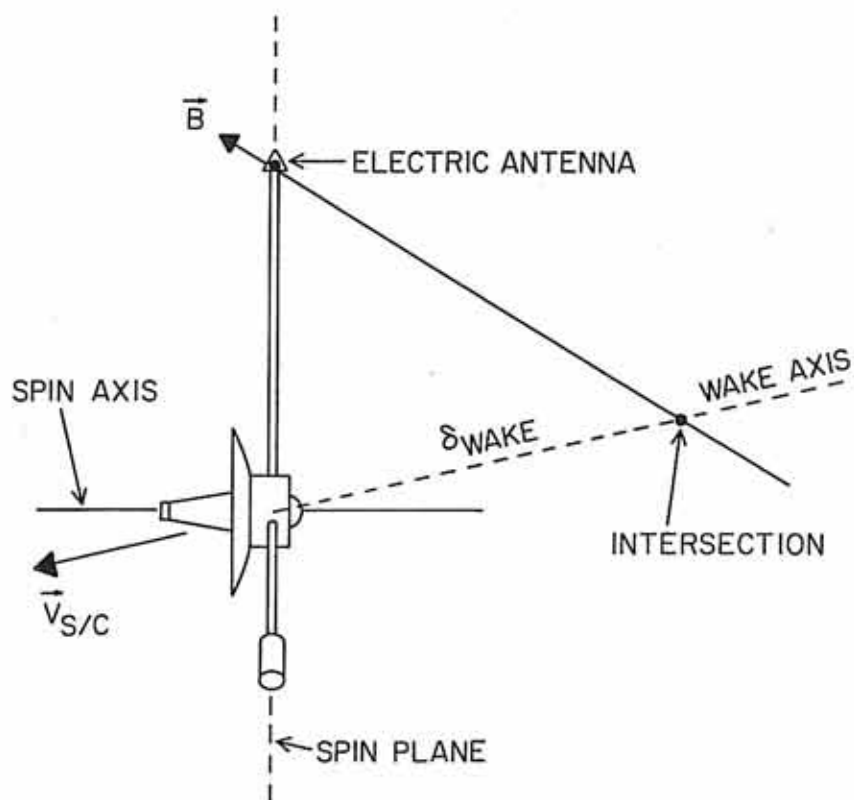
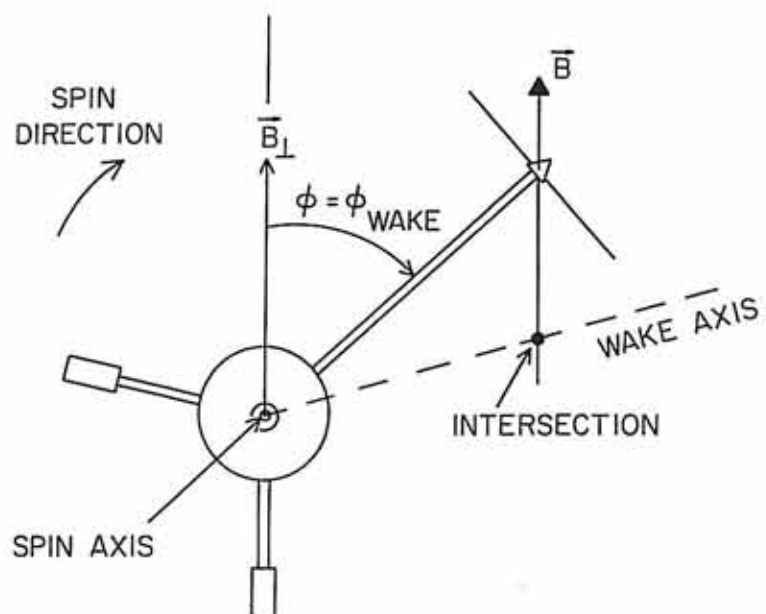


Figure 11. The spectrogram in the top panel shows the broadband electric field strength as a function of the spacecraft rotation angle and time. The field strength is plotted in color running from 3×10^{-7} (blue) to 10^{-4} (red) V/m. The white line labelled ϕ_{wake} gives the rotation angle at which the magnetic field line through the center of the electric antenna intersects the wake axis. A clearly defined enhancement occurs when $\phi \simeq \phi_{wake}$. The bottom panel shows the distance parameter, δ_{wake} , as a function of time. The discontinuities in ϕ_{wake} , at 2032:20 and 2049:50 UT, occur as the magnetic field passes through the spin plane. Note that $\delta_{wake} = 0$ at these times.

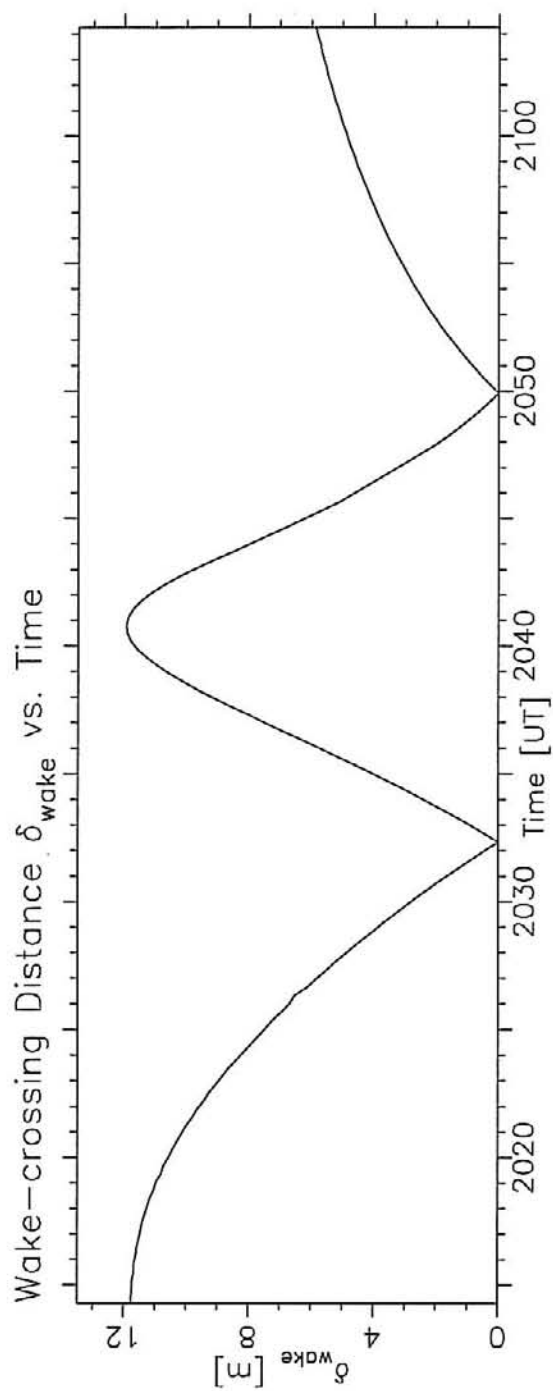
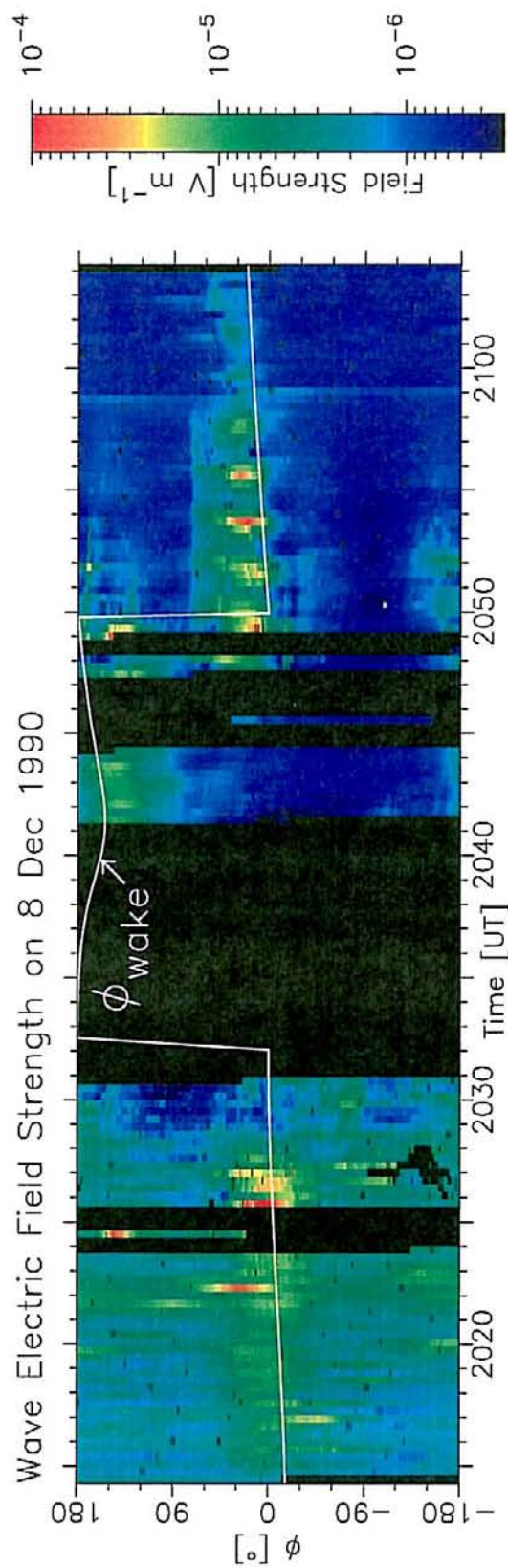


Figure 12. Side views of the (a) cylindrical and (b) conical wake models. The wake axis in each case has been inclined to the spin axis (horizontal line) by 4.5° . The wake boundaries are indicated by the dotted and dot-dashed lines.

A-G95-73

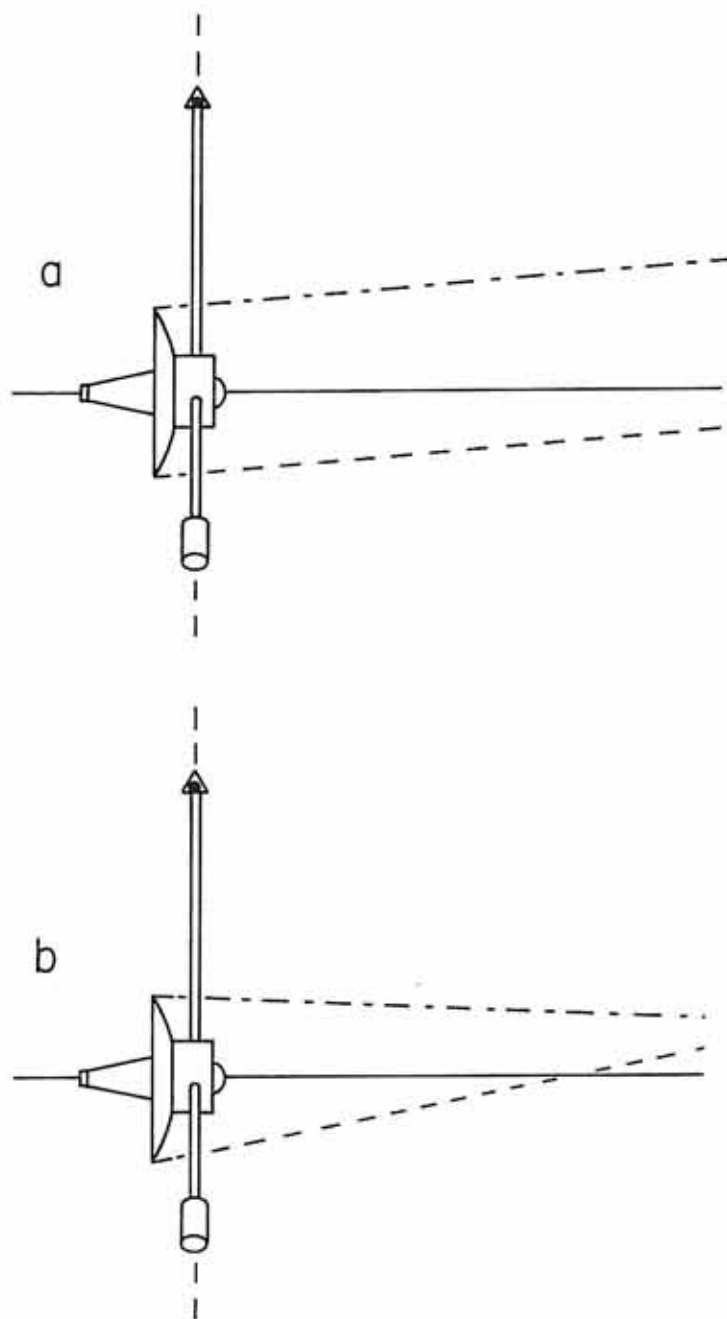


Figure 13. The spectrogram in the top panel is exactly similar to that in the top panel of Fig. 11, and the white lines give the rotation angles at which magnetic field lines through the electric antenna intersect the cylindrical wake. The bottom panel shows the distance parameter, δ_{wake} , as a function of time, for the heavy dotted and dot-dashed lines.

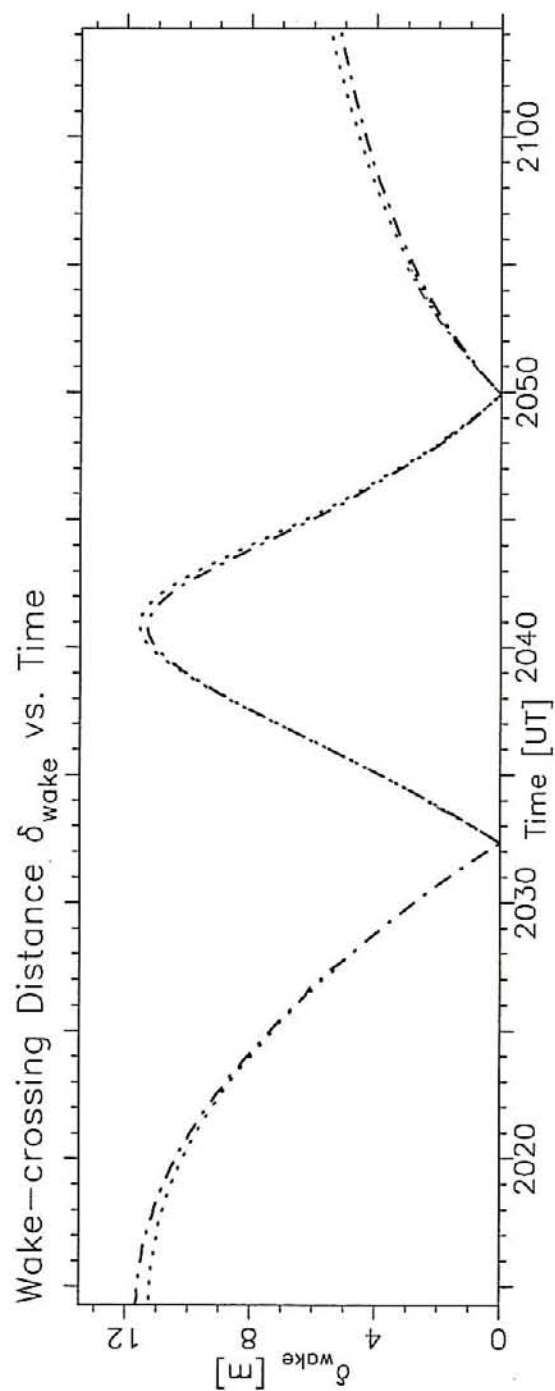
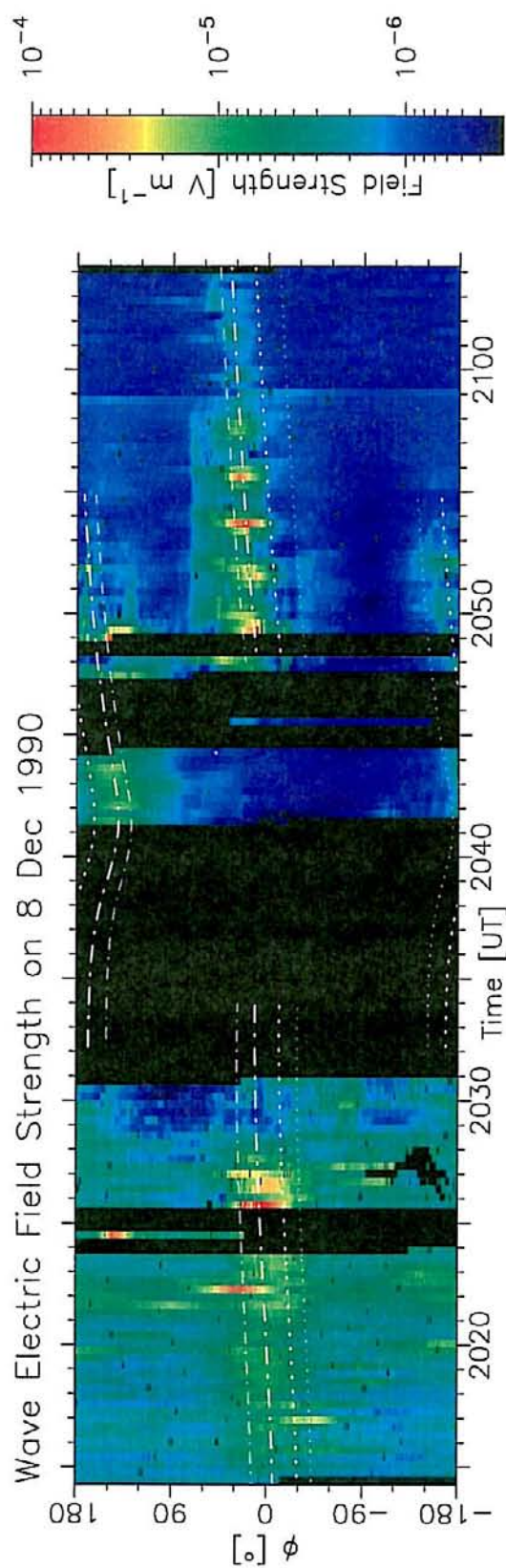


Figure 14. The spectrogram in the top panel is exactly similar to that in the top panel of Fig. 11, and the white lines give the rotation angles at which magnetic field lines through the electric antenna intersect the conical wake. The bottom panel shows the distance parameter, δ_{wake} , as a function of time, for the heavy dotted and dot-dashed lines.

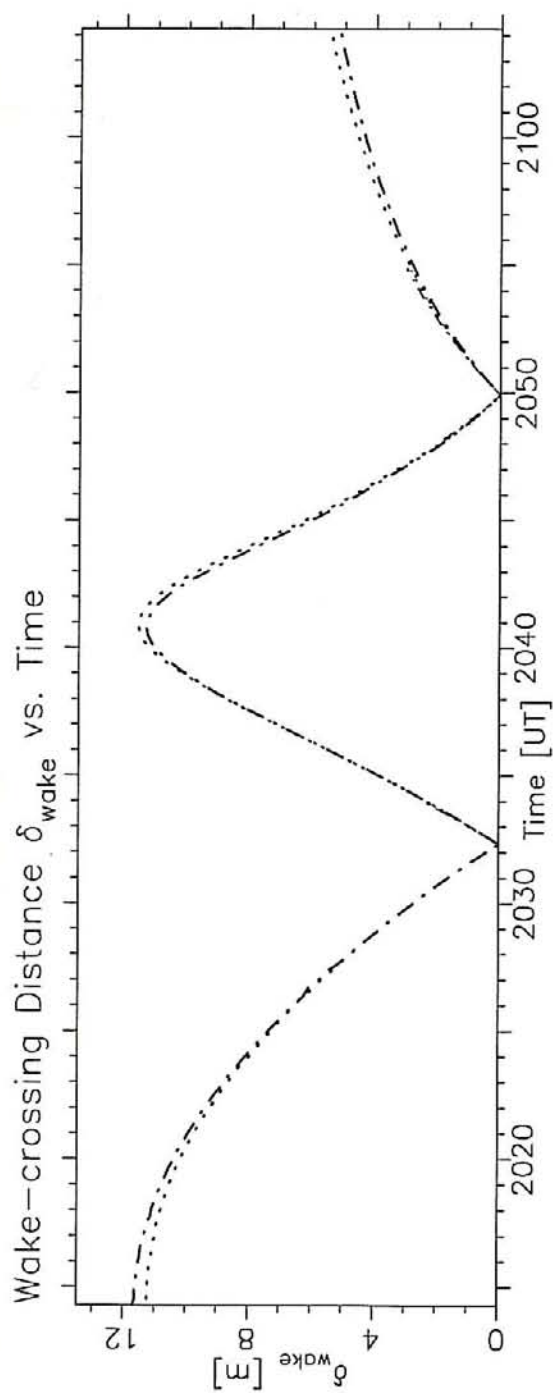
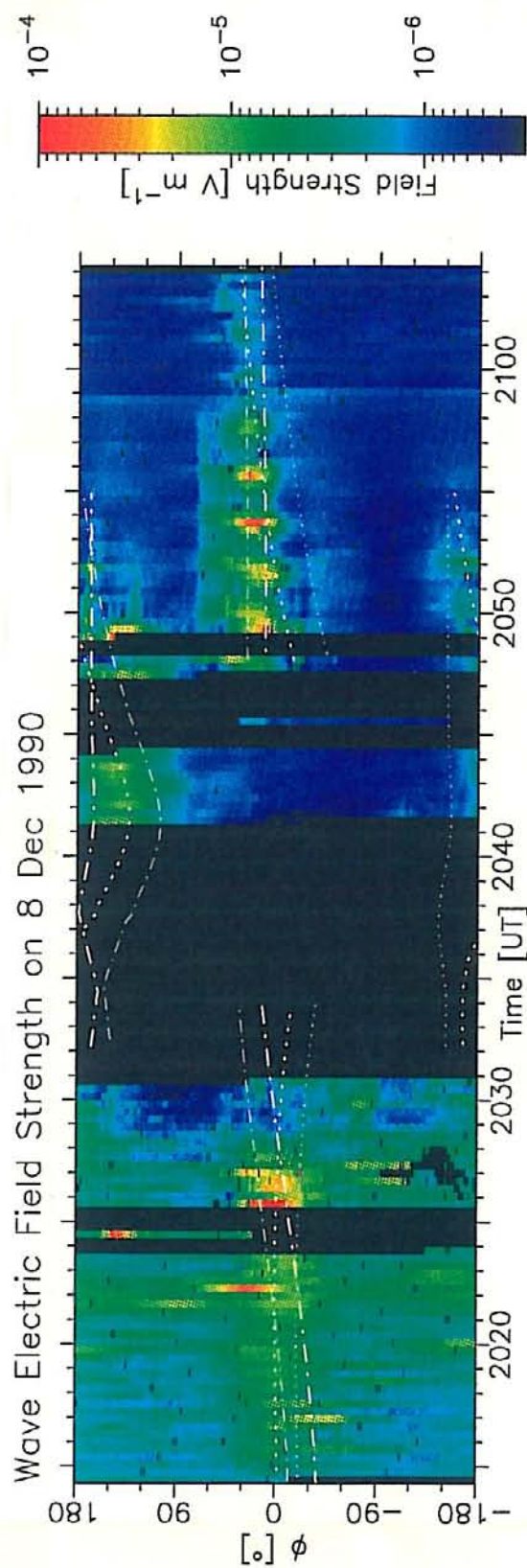


Figure 15. A side view of the cylindrical wake model, depicting the significant wake intersection geometries. The wake boundaries are again indicated by the dotted and dot-dashed lines. The antennas shown are projections of the electric antenna along magnetic field lines into the plane of the side view, each occurring at a different time and rotation angle. The heavy dot-dashed and dotted white lines in the top panels of Figures 13 and 14 correspond to rotation angles at which the wake boundary intersects the magnetic field line through center of the antenna, as depicted by antennas (b) and (c), respectively. Similarly, the light dot-dashed and dotted white lines in the top panels of Figures 13 and 14 correspond to rotation angles at which the wake boundary intersects the magnetic field line through one antenna tip, as shown by antennas (a) and (d), respectively.

A-G95-74

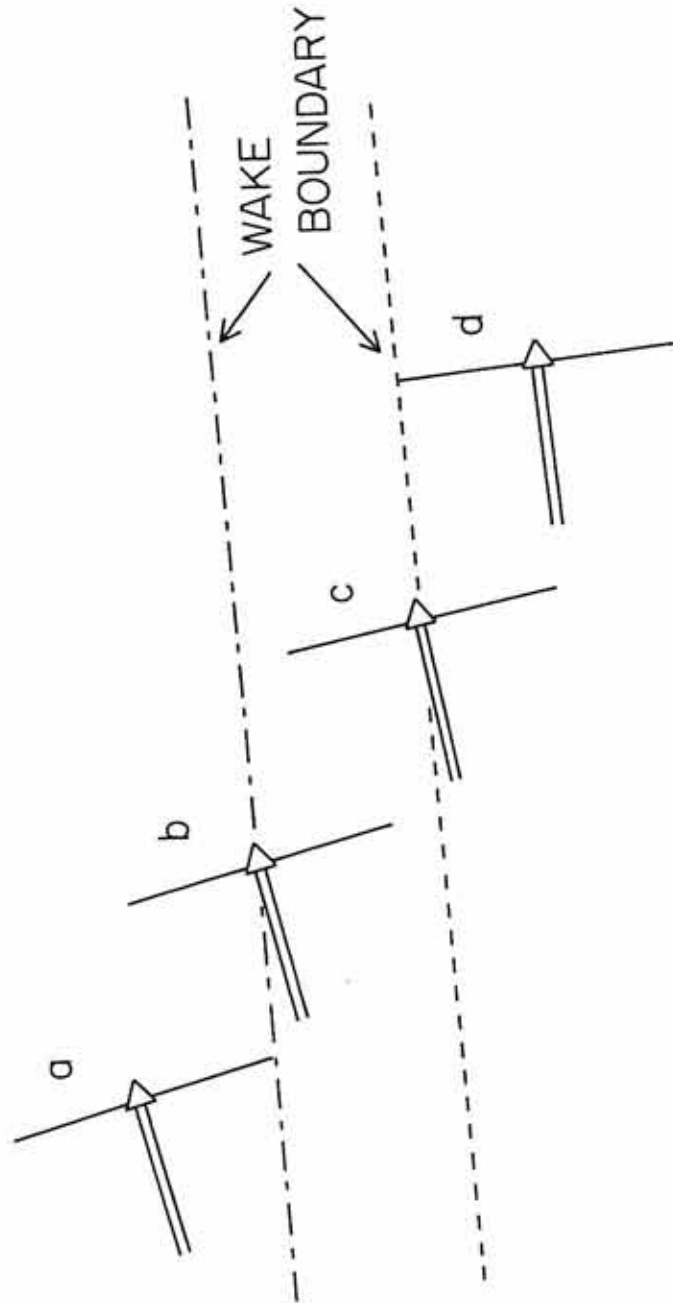


Figure 16. A plot showing the frequency (open squares) and growth rate (solid dots) for the electrostatic lower-hybrid-drift instability (LHDI) as a function of the ratio of parallel to perpendicular wavenumbers. The model assumes that \vec{B} is parallel to \hat{z} , ∇n is parallel to \hat{x} , and $\vec{E} \times \vec{B}$ is parallel to \hat{x} . The perpendicular wavenumber k_y is 12.5/m, the diamagnetic drift speed v_{dr} is 3.3×10^3 m/s, the $\vec{E} \times \vec{B}$ -drift speed v_E is 7.0×10^3 m/s, and the Larmor radius ρ_e is 0.11 m.

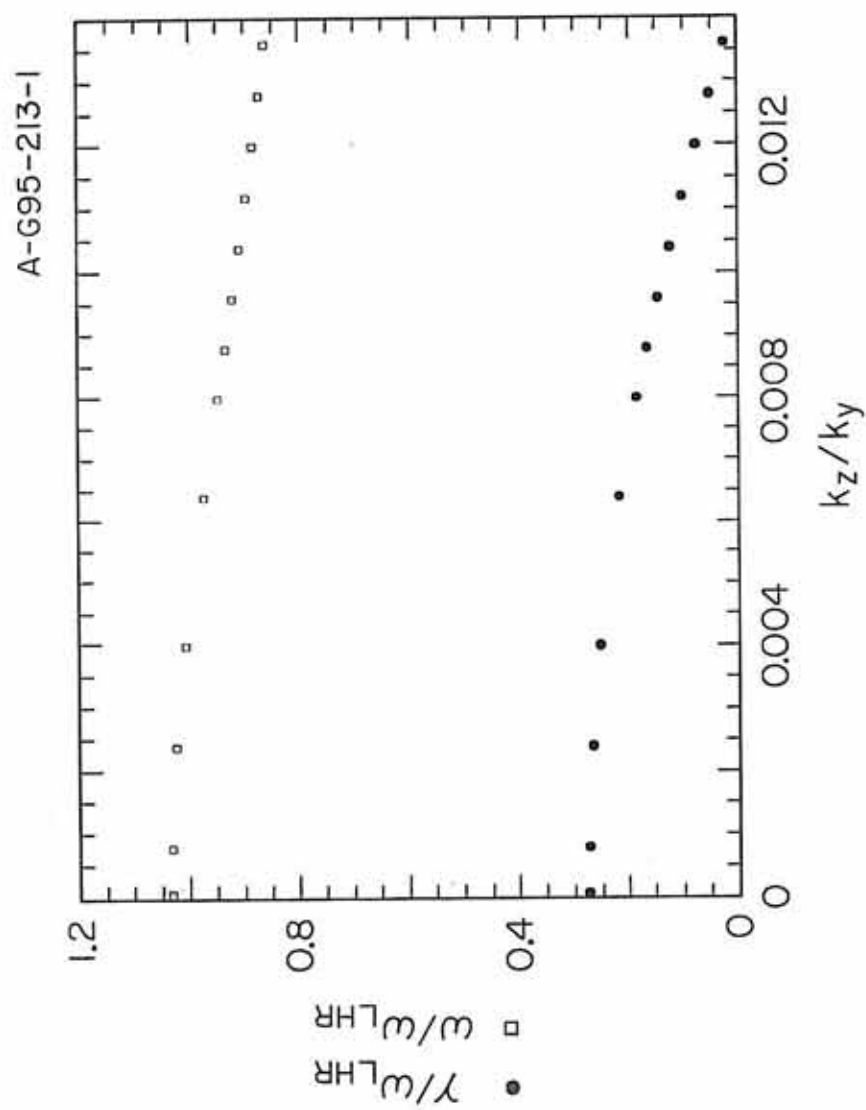


Figure 17. A plot showing the computed frequency (open squares) and growth rate (solid dots) as a function of $k_y \rho_e$ for the electrostatic LHDI. This demonstrates the dependence of ω and γ on the perpendicular wavenumber k_y . The parameters are $k_z = 10^{-7}/\text{m}$, $v_{dr} = 3.3 \times 10^3 \text{ m/s}$, $v_E = 7.0 \times 10^3 \text{ m/s}$, and $\rho_e = 0.11 \text{ m}$.

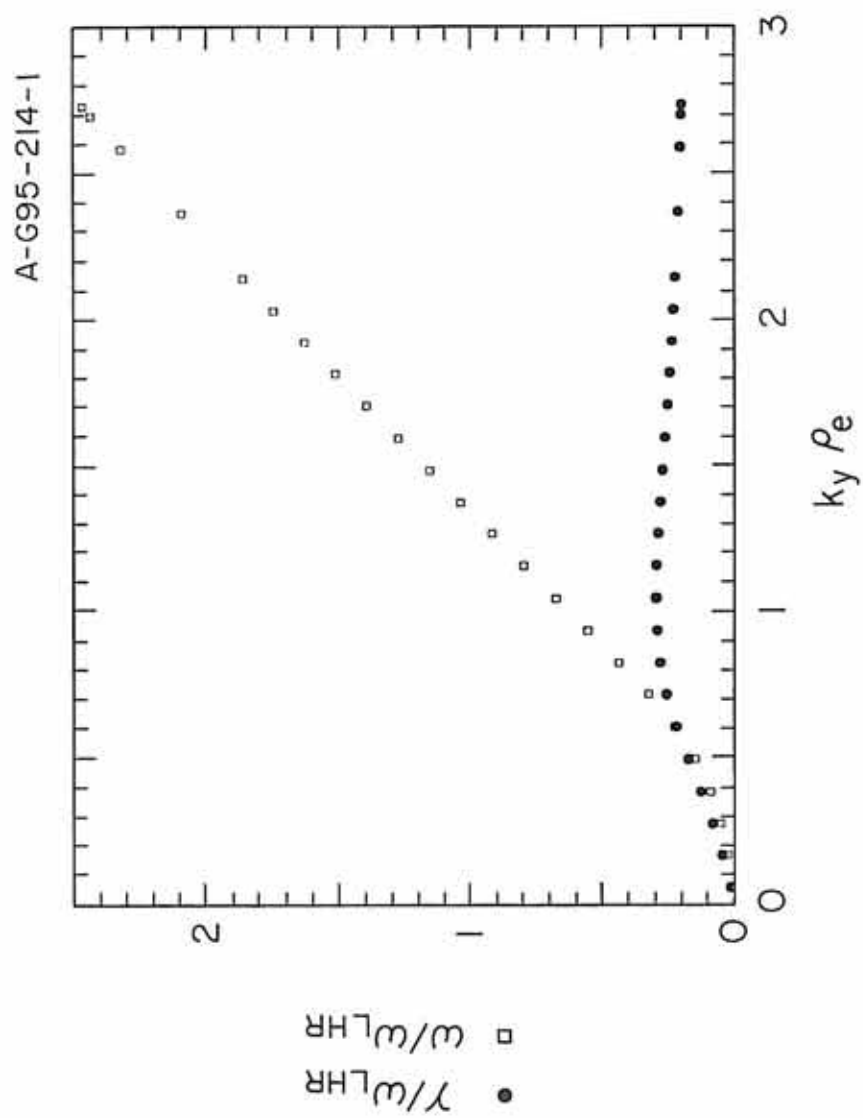


Figure 18. A plot showing the frequency (open squares) and growth rate (solid dots) for the electrostatic LHDI as a function of the diamagnetic drift speed. The parameters are $k_y = 9.512/\text{m}$ ($k_y \rho_e \sim 1$), $k_z = 10^{-7}/\text{m}$, $v_E = 7.0 \times 10^3$ m/s, and $\rho_e = 0.11$ m.

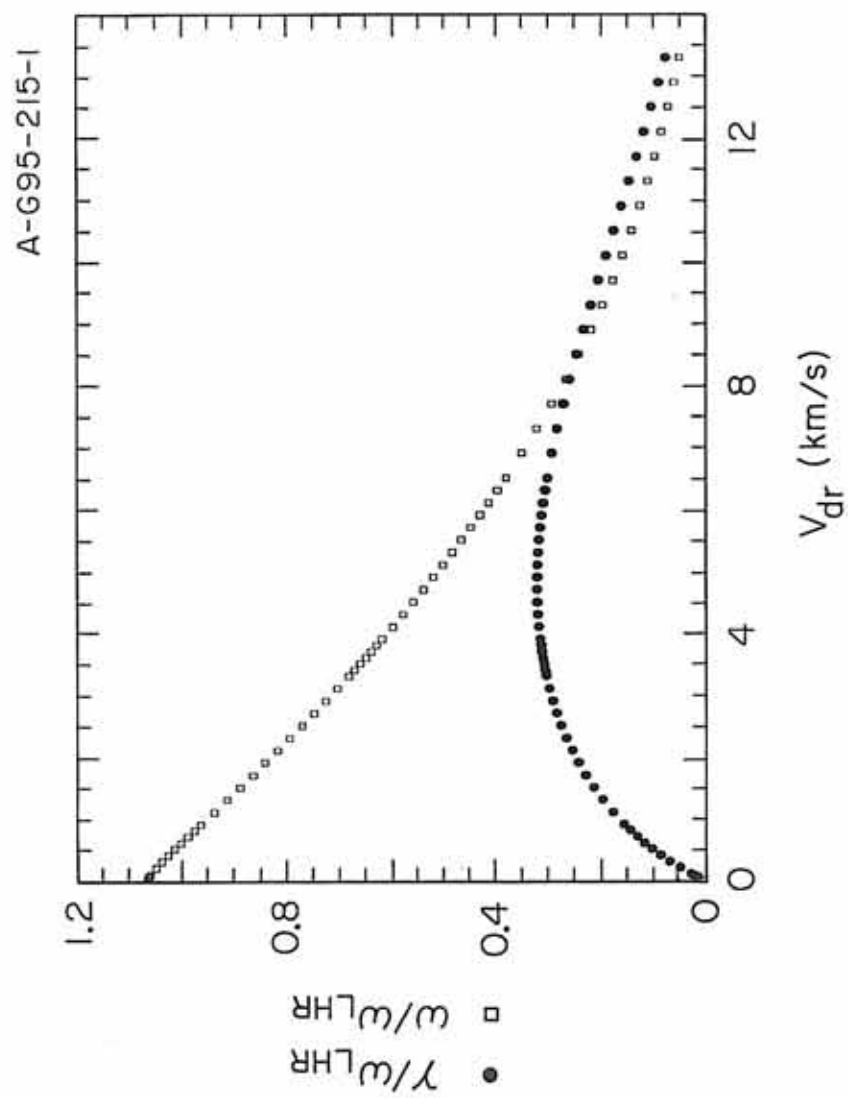


Figure 19. A plot showing the frequency (open squares) and growth rate (solid dots) for the electrostatic LHDI as a function of the $\vec{E} \times \vec{B}$ -drift speed. The parameters are $k_y = 9.512/\text{m}$ ($k_y \rho_e \sim 1$), $k_z = 10^{-7}/\text{m}$, $v_{dr} = 3.3 \times 10^3$ m/s, and $\rho_e = 0.11$ m.

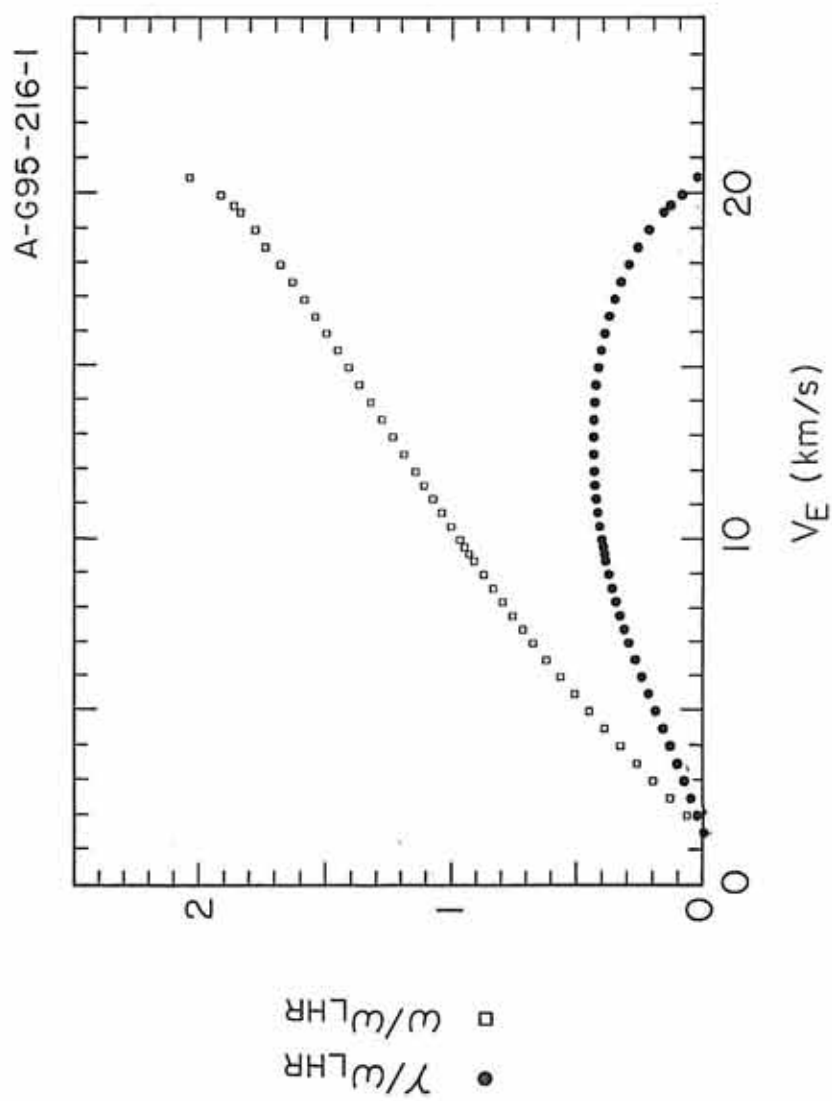


Figure 20. A plot showing the maximum value of the Doppler shift $\cos \phi$ factor as a function of time (in UT) assuming the lower hybrid wave \vec{k} is unchanged. The dependence of $\cos \phi$ on time using a cylindrical wake is plotted as a dot-dashed line, and the dependence of $\cos \phi$ on time using a conical wake is plotted as a solid line.

